The formation of supermassive black holes from Population III.1 seeds. III. Galaxy evolution and black hole growth from semi-analytic modelling

(article starts on next page)

The formation of supermassive black holes from Population III.1 seeds. III. Galaxy evolution and black hole growth from semi-analytic modelling

Vieri Cammelli [1,2,3,4]★ Pierluigi Monaco,[1,2,4,5] Jonathan C. Tan,[3,6] Jasbir Singh [7] Fabio Fontanot [2,4]
Gabriella De Lucia [2,4] Michaela Hirschmann [2,8] and Lizhi Xie [2,9]

[1]*Astronomy Unit, Department of Physics, University of Trieste, via G.B. Tiepolo 11, I-34143 Trieste, Italy*
[2]*INAF – Astronomical Observatory of Trieste, via G.B. Tiepolo 11, I-34143 Trieste, Italy*
[3]*Department of Space, Earth and Environment, Chalmers University of Technology, SE-412 96 Gothenburg, Sweden*
[4]*IFPU–Institute for Fundamental Physics of the Universe, Via Beirut 2, I-34151 Trieste, Italy*
[5]*INFN, Sezione di Trieste, Via Valerio 2, I-34127 Trieste, Italy*
[6]*Department of Astronomy, University of Virginia, Charlottesville, VA 22904, USA*
[7]*INAF–Astronomical Observatory of Brera, via Brera 28, I-20121 Milan, Italy*
[8]*Institute of Physics, Lab for Galaxy Evolution, EPFL, Observatoire de Sauverny, Chemin Pegasi 51, CH-1290 Versoix, Switzerland*
[9]*Tianjin Astrophysics Center, Tianjin Normal University, Binshuixidao 393, Xiqing, 300387 Tianjin, People's Republic of China*

ABSTRACT

We present an implementation of Pop III.1 seeding of supermassive black holes (SMBHs) in a theoretical model of galaxy formation and evolution to assess the growth of the SMBH population and the properties of the host galaxies. The model of Pop III.1 seeding involves SMBH formation at redshifts $z \gtrsim 20$ in dark matter minihaloes that are isolated from external radiative feedback, parametrized by isolation distance $d_{\rm iso}$. Within a standard ΛCDM cosmology, we generate dark matter haloes using the code PINOCCHIO and seed them according to the Pop III.1 scenario, exploring values of $d_{\rm iso}$ from 50 to 100 kpc (proper distance). We consider two alternative cases of SMBH seeding: a halo mass threshold model in which all haloes $> 7 \times 10^{10}\,{\rm M_\odot}$ are seeded with $\sim 10^5\,{\rm M_\odot}$ black holes; an all light seed model in which all haloes are seeded with low, stellar mass black holes. We follow the redshift evolution of the haloes, populating them with galaxies using the GAlaxy Evolution and Assembly theoretical model of galaxy formation, including accretion on SMBHs and related feedback processes. Here we present predictions for the properties of galaxy populations, focusing on stellar masses, star formation rates, and black hole masses. The local, $z \sim 0$ metrics of occupation fraction as a function of the galaxy stellar mass, galaxy stellar mass function, and black hole mass function all suggest a constraint of $d_{\rm iso} < 75$ kpc. We discuss the implications of this result for the Pop III.1 seeding mechanism.

Key words: black hole physics – stars: formation – stars: Population III – galaxies: active – galaxies: formation – galaxies: haloes.

1 INTRODUCTION

The origin of supermassive black holes (SMBHs) that reside in the nuclei of massive galaxies is one of the most pressing topics of current astrophysics research. A central challenge lies in explaining the large masses of the black holes observed in bright quasars (QSOs) at early cosmic epochs. For instance, Wang et al. (2021) report a $\sim 10^9\,{\rm M_\odot}$ SMBH at $z = 7.642$ which, even assuming Eddington limited accretion throughout its entire lifetime, would require a seed mass of $\sim 10^4\,{\rm M_\odot}$ at $z \sim 30$. These observations impose stringent constraints on theories of SMBH formation and growth.

How SMBHs are seeded has been the subject of numerous studies (see reviews of, e.g. Rees 1978; Volonteri 2010; Inayoshi, Visbal & Haiman 2020). Among proposed mechanisms, the *direct collapse* (DCBH) scenario advances the idea that a primordial gas cloud

hosted by a relatively massive, atomically cooled, UV-irradiated halo of $\sim 10^8\,{\rm M_\odot}$ collapses into a single supermassive star of $\sim 10^{4-6}\,{\rm M_\odot}$, subsequently forming a *massive seed* by $z \sim 10$ (e.g. Bromm & Loeb 2003; Begelman, Volonteri & Rees 2006; Montero, Janka & Müller 2012). While this mechanism can explain the number density of high redshift quasars, its strict conditions hinder the formation of sufficient numbers of SMBHs to account for the observed SMBH population at $z = 0$ (Chon et al. 2016; Wise et al. 2019). Other works indicate *light* seeds, of the order of 100 ${\rm M_\odot}$, to be byproducts of 'standard' Pop III stars forming in $\sim 10^6\,{\rm M_\odot}$ dark matter 'minihaloes' at $z \sim 20$ (e.g. Madau & Rees 2001; Tan & McKee 2004; McKee & Tan 2008). Moreover, very dense star clusters at high z may dynamically evolve leading to the formation of *intermediate*-mass black hole (IMBH) seeds with $10^{2-4}\,{\rm M_\odot}$ (e.g. Portegies Zwart et al. 2004; Devecchi & Volonteri 2009).

One challenge facing models that start with light or intermediate-mass seeds is the apparent dearth of observed IMBHs in the local Universe (Banik, Tan & Monaco 2019; Greene, Strader & Ho 2020;

★ E-mail: vieri.cammelli@phd.units.it

Volonteri, Habouzit & Colpi 2021). In addition, it is difficult to model the IMBH seeding in a cosmological context, unless requiring either sub-grid or probabilistic recipes calibrated on high-resolution zoom simulations as recently studied by Bhowmick et al. (2024b,c).

An alternative scenario of SMBH formation from Pop III.1 protostars has been studied in a cosmological context by Banik et al. (2019) (hereafter Paper I) and Singh, Monaco & Tan (2023) (hereafter Paper II). Pop III.1 sources are defined as special Pop III stars forming at the centre of dark matter (DM) minihaloes in the early Universe ($z \gtrsim 20$), which are isolated from any source of stellar or SMBH feedback (McKee & Tan 2008). This criterion is parametrized by an isolation distance $d_{\rm iso}$, expressed in physical units, of the order of $\lesssim 100 \, {\rm kpc}$. The physical mechanism that allows growth of Pop III.1 protostars to high mass, i.e. $\gtrsim 10^4 \, {\rm M}_\odot$, is the influence of dark matter annihilation (DMA) on the protostellar structure (Spolyar, Freese & Gondolo 2008; Natarajan, Tan & O'Shea 2009; Freese et al. 2010; Rindler-Daller et al. 2015). The fiducial assumption is that dark matter is composed of a weakly interacting massive particles (WIMPs), which undergoes self-annihilation with a weak interaction cross-section. If sufficient WIMPs are captured by the Pop III.1 protostar, then its structure is altered. In particular, the protostar can remain relatively large as it accretes to high masses, thus reducing its ionizing feedback on its own accretion flow. This may enable the efficient accretion of a large fraction of the entire baryonic content of the parent minihalo, i.e. $\sim 10^5 \, {\rm M}_\odot$, to the Pop III.1 protostar, which subsequently, within a few Myr, collapses to a SMBH. Other minihaloes are Pop III.2 sources, i.e. still metal free, but, having been irradiated by UV radiation, have higher free electron abundances leading to greater abundances of H_2 and HD, higher cooling rates, and fragmentation to lower mass, $\sim 10 \, {\rm M}_\odot$, stars (Greif & Bromm 2006; Johnson & Bromm 2006).

The Pop III.1 model thus predicts a characteristic mass of $\sim 10^5 \, {\rm M}_\odot$ for SMBH seeds and provides an explanation for the apparent dearth of IMBHs. In addition, the Pop III.1 model predicts that SMBHs form very early in the Universe, which provides a theoretical explanation for the population of high-z SMBHs without the need for sustained Eddington or super-Eddington levels of accretion. Another prediction is that the initial spatial distribution of SMBHs is relatively uniform, i.e. with low levels of clustering, with the seeds separated from each other by distances of order $d_{\rm iso}$. The co-moving number density of SMBHs, $n_{\rm SMBH}$, is sensitive to $d_{\rm iso}$, with a value of about $100 \, {\rm kpc}$ (proper distance) able to explain the observed local number density of SMBHs of $\sim 5 \times 10^{-3} \, {\rm Mpc}^{-3}$. The value of $d_{\rm iso}$ also sets a limit on the formation epoch of SMBHs. For $d_{\rm iso} = 50 - 100 \, {\rm kpc}$, most seeds are formed at $z \sim 30$, i.e. with co-moving separations of $\sim few$ Mpc, and the process is largely complete by $z \sim 25$, after which $n_{\rm SMBH}$ is nearly constant. This time-scale has a weak dependence on $d_{\rm iso}$, with later seeding happening for smaller $d_{\rm iso}$. As a result of the initially separated distributions, in the Pop III.1 model mergers only begin to occur at relatively late times, i.e. $z \lesssim 1$, which causes $n_{\rm SMBH}$ to decrease by modest amounts $\sim 10 - 20$ per cent (Singh et al. 2023). Consequently, the SMBH number density remains fairly constant down to the local Universe, with only a small fraction of seeds lost in halo mergers by $z = 0$. At redshifts > 5, this model makes strong predictions for the number of SMBHs we expect in the early Universe (e.g. their relative contribution to the luminosity functions), underscoring the importance of current and future deep field observations of high redshift AGNs. Such observations are crucial for potentially distinguishing among different seeding mechanisms and/or accretion schemes. Furthermore, by redshift 0 the occupation fraction of seeded haloes saturates to unity for the most massive haloes as a function of the isolation distance $d_{\rm iso}$.

Numerical simulations of galaxy formation and evolution in cosmological volumes typically have quite limited spatial resolution and so struggle to capture the processes leading to SMBH seeding. The lack of knowledge about the physical processes and the difficulty to treat them from first principles further limit such numerical approaches. In addition, the real challenge resides in simultaneously simulating a broad range of scales, from mini-haloes at $z \sim 20 - 30$ up to the structures we observe in the local Universe. Thus, implemented seeding schemes are generally based on simple threshold models. In particular, many works seed a SMBH once the parent halo reaches a certain threshold in dark matter mass, i.e. a halo mass threshold (HMT) seeding scheme (Sijacki et al. 2007; Matteo et al. 2008). The same idea has been used by Vogelsberger et al. (2014) within the Illustris Project, as well as in the Evolution and Assembly of GaLaxies and their Environments (EAGLE) simulations of Barber et al. (2016).

Extending to alternative threshold models, in the HORIZON-active galactic nucleus (AGN) simulation (with DM mass resolution of $8 \times 10^8 {\rm M}_\odot$), Volonteri et al. (2016) implemented lower limits for gas and stellar densities, as well as stellar velocity dispersion, to determine if a galaxy hosts a black hole, using a seed mass of $10^5 \, {\rm M}_\odot$. Their formation was restricted to redshifts $z > 1.5$ and all forming black holes had to be separated by at least 50 comoving kiloparsecs to prevent multiple black holes from forming in the same galaxy. Similarly, the OBELISK simulation (Trebitsch et al. (2021), based on a subvolume of the HORIZON-AGN simulation) used a slightly lower seed mass and applied gas and stellar density thresholds, including gas Jeans instability, requiring an isolation of $50 \, {\rm kpc}$ from other SMBHs to prevent multiple black hole formation. In another approach, the ROMULUS simulation (Tremmel et al. (2017), particle DM mass $\sim 3 \times 10^5 {\rm M}_\odot$) set criteria based on metallicity limits, gas density thresholds, and a restricted temperature range for SMBH formation, using a seed mass of $10^6 \, {\rm M}_\odot$. Additionally, in the Illustris Project framework, Bhowmick et al. (2022) explored various gas-based SMBH seeding prescriptions and a range of seed masses from around 10^4 to $10^6 \, {\rm M}_\odot$, while keeping a relatively high DM resolution about $\sim 6 \times 10^6 {\rm M}_\odot$. Moreover, in high-resolution zoom simulations Bhowmick et al. (2024a,b,c) explicitly resolved pristine and dense gas clouds forming $\sim 10^3 \, {\rm M}_\odot$ seeds and built a stochastic seeding scheme that can directly set the initial seeding conditions in lower resolution runs. Using the hydrodynamical cosmological code RAMSES, Habouzit et al. (2016) investigated the conditions under which haloes can host DCBHs over a large range of resolutions and box sizes as a function of the illuminating Lyman–Werner (LW) background and supernova (SN) feedback. Under optimistic assumptions, their SMBH number density ranges from 7×10^{-7} up to $10^{-4} \, {\rm cMpc}^{-3}$, still a factor of at least ~ 10 lower than the local estimate. Despite the improvements in the treatment of subgrid physics and the implementation of zoom-in approaches, large, cosmological simulations do not include yet a full physical model for SMBH formation (e.g. see Di Matteo, Angles-Alcazar & Shankar 2023).

A complementary approach with respect to hydrodynamical simulations is provided by semi-analytic models (SAMs). SAMs are tools used to simulate the evolution of galaxy populations within dark matter haloes (DMHs) by modelling the physical processes that drive the evolution of the baryonic components of dark matter haloes by invoking theoretically and/or observationally motivated prescriptions. We stress here that such prescriptions (*sub-grid* physics) are similarly implemented in hydrodynamical simulations.

These processes encompass baryonic gas cooling and heating, star formation, gas accretion onto SMBHs, and their related feedback mechanisms. The flexibility of these models permits us to obtain predictions of galaxy properties across cosmological volumes and allows efficient exploration of the associated parameter space in order to study the impact of different physical assumptions [for a review see Somerville & Davé (2015); De Lucia (2019)]. On the other hand, the price to pay is the lack of a complete and consistent treatment of the gas hydrodynamics. One limitation of the application of SAMs to the study of the early BH seeding lies in the lack of resolution in dark matter halo trees generated with either N-body simulation or analytic recipes such as Press & Schechter (1974) and Lacey & Cole (1993). In fact, dealing with cosmological volumes significantly impacts the modelling of BH seed formation, which depends on the local gas conditions within haloes and the DM mass resolution.

Among the BH seeding mechanisms implemented in SAMs, Ricarte & Natarajan (2018) used DCBHs whose mass is calculated proportionally to the DM halo mass. Given their redshift-dependent mass resolution scheme, this results in placing $\gtrsim 10^4 \, M_\odot$ BH seeds at $z \sim 15 - 20$ in parent haloes of minimum mass about $5 \times 10^6 \, M_\odot$. In the Cosmic Archaeology Tool (CAT) presented in Trinca et al. (2022), both light seeds from Pop III stars and DCBHs are considered to study their contribution to the BH mass function. Similarly, BH seed masses ranging from 10^2 up to $10^5 \, M_\odot$ were assigned in the DELPHI SAM (Dayal et al. 2019) according to the probability of a halo to host a DCBH or a stellar BH remnant. Sassano et al. (2021) seeded BHs at the centre of galaxies based on the locally derived properties of the halo environment. In particular, several thresholds for the illuminating LW flux, the metallicity and the gas-to-dust ratio were used to determine whether the final BH would be a light, medium, or heavy seed. In the L-GALAXIES model, Spinoso et al. (2023) studied DCBHs according to spatial variations of the star formation in terms of chemical and radiative feedback. Since the first mini-haloes ($T_{vir} \sim 10^3 \, K$) lie below their resolution limit, Pop III remnant seeds were placed following the sub-grid approach of Sassano et al. (2021).

In this paper, we model SMBH formation in a cosmological box within the standard ΛCDM cosmogony by exploiting halo merger trees generated with PINOCCHIO (Monaco, Theuns & Taffoni 2002; Munari et al. 2017) to simulate the large-scale distribution of DMHs. The PINOCCHIO code follows the evolution of cosmic perturbations and structures based on Lagrangian perturbation theory (LPT), ellipsoidal collapse, and excursion-set theory and generates catalogues of collapsed objects (i.e. DMHs). Subsequently, these haloes are seeded according to their isolation state at the formation time (see Paper I and Paper II). By adapting the PINOCCHIO DMH merger tree to a suitable format, we follow the redshift evolution of these structures and we populate them with galaxies utilizing the state-of-the-art GAlaxy Evolution and Assembly (GAEA) semi-analytic model (SAM) of galaxy formation and evolution (Hirschmann, De Lucia & Fontanot 2016; Fontanot et al. 2020; De Lucia et al. 2024). Different seeding mechanisms can be explored in this framework, but in this study we focus mainly on the Pop III.1 model. We note here that the two key tools that we use in our approach have been successfully tested against observational and numerical measurements: (i) the GAEA model is able to reproduce a wide range of observational results at $z = 0$ and up to $z \sim 5$; (ii) the high resolution realizations of halo merger trees constructed with PINOCCHIO result from an approximate method which has been shown to agree well with simulations down to $z = 0$, as shown in the above cited papers and references therein. Note that PINOCCHIO merger trees converge with a better accuracy with respect to analytic-based

ones whose implementation in recent works are not well tested below z~4.

This paper is organized as follows. In Section 2, we describe in detail our new fully semi-analytic approach and the implementation of SMBH seeding and accretion. The main results of this study, together with the possible implications, are presented in Section 3. Finally we present our summary and conclusions in Section 4. A companion follow-up paper (Cammelli et al., in preparation) will present predictions for the luminosity functions of the galaxies and AGN and their comparison with observational data.

2 METHODS

In this work, we couple DMH merger trees extracted from cosmological boxes simulated using the PINOCCHIO algorithm with the GAEA SAM, providing predictions of the properties of galaxy populations associated with the DMH distribution at various redshifts. Given the full semi-analytic approach, we can explore wide ranges of physical and/or observational properties of galaxies with flexibility in the choice of the parametrizations adopted for the physical processes at play. In the following, we give a brief description of the PINOCCHIO runs and the GAEA model. We then describe how we interface the two codes. We design a specific code which takes the PINOCCHIO haloes as inputs, models the physical properties of main and subhaloes and returns DMH merger trees structurally equivalent to numerically derived ones. We focus our implementation on different assumptions for SMBH seeding mechanisms within the treatment of accretion modes onto the central black hole already implemented in GAEA (Fontanot et al. 2020).

In this paper we adopt the following nomenclature. Gravitationally bound DM structures that are not hosted by a larger bound structure are called *haloes*, the galaxies lying at their centres are called *central galaxies*. Haloes may host smaller bound clumps of DM, we call them *subhaloes*, and the galaxies at their centre *satellite galaxies*. In a simulation, the disruption of a subhalo may happen before the actual merger should take place, due to limited resolution. Therefore, its associated satellite can exist for some time after the disappearance of its subhalo; in this phase it is named *orphan galaxy*.

2.1 The dark matter skeleton: PINOCCHIO

PINOCCHIO (PIN-pointing Orbit Crossing-Collapsed HIerarchical Objects; Monaco et al. 2002; Munari et al. 2017) is a semi-analytic code that follows the formation and merger history of dark matter haloes in Lagrangian space, that is the space defined by the initial positions of mass elements. One can think of PINOCCHIO as an algorithm applied to the initial conditions of a simulation, where the Lagrangian space is discretized into a grid and each cell is represented by a massive particle. First, an algorithm based on ellipsoidal collapse computes, for each particle, the time at which the particle is deemed to reach a multistream region (orbit crossing). The particles are then grouped into massive haloes, whose position is estimated using LPT. As such, this code can be seen as a halo finder in Lagrangian space, that provides relatively accurate halo catalogues without running a full numerical simulation. While memory requirements are still high, so that a massive run requires a supercomputer, the computational cost is thousands time lower than an equivalent N-body simulation.

For this paper we use the PINOCCHIO run presented in Paper II of this series, Singh et al. (2023), i.e. a cubic box of side 59.7 Mpc (40 h^{-1} Mpc with $h = 0.67$) with standard Planck cosmology (Planck Collaboration VI 2020), sampled with 4096^3 particles, for a particle mass of $1.23 \times 10^5 \, M_\odot$. The smallest resolved haloes

were set at 10 particles (an acceptable value for a semi-analytic algorithm), i.e. $1.23 \times 10^6 \, M_\odot$. This box was processed in Paper II to compute which mini-haloes host SMBH seeds in the Pop III.1 scenario, with fiducial seed mass assumed to be $10^5 M_\odot$. Distributing such a large box on hundreds of nodes makes it difficult to reconstruct massive haloes, whose Lagrangian size may be similar or even exceed the size of a computational domain. As explained in Paper II, for evolution from $z = 10$ down to $z = 0$ the box was re-run at a lower resolution (using 1024^3 particles) on a single node, thus avoiding any issue in the domain decomposition, and the information about which haloes are seeded was propagated in Lagrangian space by assigning the seeds to the lower resolution particle that contains the seeded mini-halo. In the low-resolution run (used in this work), the dark matter particle mass is $\sim 5 \times 10^7 \, M_\odot$, and the smallest resolved halo is a factor of 10 more massive. PINOCCHIO is also able to produce the merger history of dark matter haloes with continuous time sampling by providing the exact redshift for each individual merger event.

2.2 GAEA semi-analytic model

GAEA represents an evolution of the original model published by De Lucia & Blaizot (2007). In this study, we utilize the version of the model published in Fontanot et al. (2020, hereafter F20). The model includes: (a) a comprehensive treatment of chemical enrichment, explicitly addressing differential enrichment linked to asymptotic giant branch (AGB) stars, Type II SNe, and Type Ia SNe (De Lucia et al. 2014); (b) an updated approach to stellar feedback tracing gas ejection via stellar-driven outflows (the model is partially based on results from hydrodynamical simulations; Hirschmann et al. 2016) coupled with a gas re-incorporation time-scale dependent on DMH mass (Henriques et al. 2015); (c) an improved model for disc sizes (Xie et al. 2017) tracking angular momentum evolution through mass and energy exchanges within the galaxy; (d) an update modelling for cold gas accretion onto SMBHs (F20). This latter ingredient is relevant for this study and will be described in more detail in the next subsection.

GAEA has been shown to reproduce a wide range of observations. Fontanot, Hirschmann & Lucia (2017b) demonstrated that the evolution of the galaxy stellar mass function (GSMF) and cosmic star formation rate (SFR) obtained from GAEA are in agreement with measurements available up to $z \sim 7$. Hirschmann et al. (2016) showed that the model reproduces well the observed gas fractions and mass-metallicity relations at $z < 3$, but tends to overpredict the SF activity of low-mass galaxies at low redshift. The model we use in this study also nicely reproduces the fraction of quiescent galaxies as a function of stellar mass and hierarchy at low-z (De Lucia, Hirschmann & Fontanot 2019). Furthermore, the model galaxies exhibit size–mass and angular momentum–mass relations that are in relatively good agreement with observational assessments, both in the local Universe and at higher redshifts (Zoldan et al. 2019). In future work we will extend our analysis to alternate recent versions of the model including distinct treatments for the partitioning of cold gas into atomic and molecular hydrogen (Xie et al. 2017, 2020; De Lucia et al. 2024), as well as a model accounting for a variable stellar initial mass function (Fontanot et al. 2017a, 2018, 2024). However, these two variations will not be considered in the present study.

2.2.1 SMBH accretion and feedback

The modelling adopted in GAEA for the accretion onto the SMBH is described in detail in F20. We note here that this phenomenon is

treated following two main specific prescriptions. A first accretion channel from hot gas, known as *radio-mode*, is modelled according to the implementation of Croton et al. (2006). In this mode, the accretion rate is proportional to the mass of the BH ($M_{\rm BH}$), to the virial velocity $V_{\rm vir}$ and to the fraction of the hot gas in the DMH ($f_{\rm hot}$), adjusted by a free parameter $k_{\rm radio}$:

$$\dot{M}_{\rm R} = k_{\rm radio} \frac{M_{\rm BH}}{10^8 M_\odot} \frac{f_{\rm hot}}{0.1} \left(\frac{V_{\rm vir}}{200 \, {\rm km\, s^{-1}}} \right)^3. \tag{1}$$

However, the more luminous AGNs arise from a second accretion mode, traditionally termed the *QSO-mode*: in particular we take advantage of the modelling of cold gas accretion onto SMBHs presented in F20. In particular, we refer to the model implementation defined as F06-GAEA in F20, which is based on prescriptions first described by Fontanot et al. (2006). The occurrence of the AGN phenomenon has been accomplished by using a three phase approach. (1) The first phase requires that a fraction of the cold gas available in the galaxy dissipates a substantial amount of angular momentum and gathers in the central region, turning into a gas reservoir available for accretion onto the BH. (2) The amount of cold gas flowing from the reservoir towards the centre of the galaxy leads to accretion onto the BH. (3) Ultimately, outflows induced by the AGN lead to the expulsion of a portion of the galaxy's gas content.

This model assumes that disc instabilities and galaxy mergers lead to an efficient angular momentum loss and trigger QSO-mode accretion events. Typically this loss of angular momentum results from SFR episodes in the central regions, which inject turbulence and exert radiation drag. We assume that, following merger events, the BH reservoir accretion rate is proportional to the central SFR via the free parameter $f_{\rm lowJ}$ schematized as:

$$\dot{M}_{\rm rsv}^{\rm cs} = f_{\rm lowJ} \psi_{\rm cs}, \tag{2}$$

with $\psi_{\rm cs}$ estimated via the collisional starburst prescriptions from Somerville, Primack & Faber (2001) and it equals the amount of SFR in the central regions triggered by the merger itself. It is important to note that BHs are assumed to merge instantaneously (no delay is assigned) once the host galaxies have merged.

For disc instabilities, the net result in GAEA involves moving a fraction of stars from the stellar disc to the stellar bulge so as to restore stability (De Lucia et al. 2011). Since there is no star formation associated by construction, we assume the reservoir growth rate to be proportional to the bulge grow rate $\dot{M}_{\rm bulge}$. Hence:

$$\dot{M}_{\rm rsv}^{\rm di} = f_{\rm lowJ} \mu \dot{M}_{\rm bulge}, \tag{3}$$

where the free parameters $f_{\rm lowJ}$ and μ (6×10^{-3} and 10, respectively, as in F20) regulate the fraction of gas accreted due to angular momentum loss.

Once the reservoir gathers gas around the central BH, accretion episodes can be triggered. Following the viscous accretion rate derived by Granato et al. (2004), we define the accretion onto the BH as:

$$\dot{M}_{\rm BH} = f_{\rm BH} \frac{\sigma_{\rm B}^3}{G} \left(\frac{M_{\rm rsv}}{M_{\rm BH}} \right)^{3/2} \left(1 + \frac{M_{\rm BH}}{M_{\rm rsv}} \right)^{1/2}, \tag{4}$$

where $\sigma_{\rm B}$ is the velocity dispersion of the bulge component, assumed to scale linearly with $V_{\rm vir}$ as derived by Ferrarese (2002) for a sample of local galaxies.

This prescription, once coupled with the amount of gas accumulated into the reservoir, can induce accretion rates beyond the Eddington limit. We limit the actual accretion rate to:

$$\dot{M}_{\rm max} = 10 \frac{M_{\rm BH}}{t_{\rm edd}} = 10 \dot{M}_{\rm edd}, \tag{5}$$

where $\dot{M}_{edd}$ is the accretion rate of a BH shining at the Eddington luminosity with a radiative efficiency of 10 per cent, over an Eddington–Salpeter time-scale $t_{edd} \simeq 45$ Myr. This upper limit is supported by both observational and theoretical findings (see e.g. Jiang, Stone & Davis 2019; Takeo et al. 2019; Delvecchio et al. 2020). Some theoretical models indicate that such large accretion rates may occur via intermittent bursts, particularly at higher redshifts (e.g. Inayoshi, Haiman & Ostriker 2016).

F20 examined the impact of AGN activity on the host galaxy, specifically focusing on its cold gas phase. AGNs are believed to influence the surrounding medium by actively heating it, and eventually leading to the expulsion of cold gas via galactic winds driven by the AGN. SNe explosions combined with the radiation pressure of the AGN are assumed to promote further accretion by compressing part of the ISM ($f_{cen} \sim 10^{-3}$) in the central region. This material is eventually added to the BH reservoir (see Monaco & Fontanot 2005). Each accretion episode described by equation (4) triggers an AGN-driven outflow, with a rate that is modelled assuming a scaling relation with the BH accretion rate:

$$\dot{M}_{qw} = \epsilon_{qw}\dot{M}_{BH}, \qquad (6)$$

where ϵ_{qw} is a free parameter which value is 320 as reported by F20. Note that this AGN-driven wind scaling shows results consistent with both hydrodynamical cosmological simulations (Brennan et al. 2018) and observational findings (Fiore et al. 2017).

2.3 Building the merger trees

The standard GAEA runs have been defined on DMH merger trees extracted from the Millennium Simulation suite (Springel et al. 2005). The merger tree format adopted in GAEA is organized as follows. The starting point is a temporal sequence of *snapshots*, where the position and velocity of all particles at a given time is provided. First, DM haloes are identified using a classical Friends-of-Friends (FoF) algorithm. Then, a second algorithm (SUBFIND) identifies subhaloes in each FoF group. Finally, the merger trees are built by identifying unique descendants for all subhaloes (see Springel et al. 2005 for details). For each identified halo or subhalo, pointers and physical quantities are stored at the same redshifts of the snapshots. These merger trees are then provided to GAEA as a skeleton for the galaxy formation model.

At the resolution of the Millennium simulation, dark matter subhaloes *disappear*, i.e. cannot be identified anymore as distinct subhaloes, at typically large distances from the halo centre, when the merger is likely incomplete. Since the baryons are more centrally concentrated than dark matter, this time is presumably underestimating the time at which the hosted satellite galaxy is expected to merge with the central galaxy. In GAEA, this numerical effect is mitigated by modelling orphan galaxies: when a subhalo is lost, its satellite galaxy is assigned a residual merger time, estimated using dynamical friction arguments, and its evolution is followed until it merges with the central galaxy of the host halo. The position and velocities of orphan galaxies are obtained by following the most bound particle of the disrupted subhalo.

The formalism and the structure of the PINOCCHIO merger trees (see Section 2.1) are substantially different compared to the numerical ones. The outputs are provided in the form of merging histories and catalogues of dark matter haloes. The merging histories offer a continuous time sampling that uniquely determines the evolution of every single halo along the merger tree, providing the mass, the redshift of first appearance, the merging redshift (if any), the halo ID, and other useful pointers. The catalogues supply, according to a time

grid, the information about mass, position, velocity, and halo ID for all haloes. Thus, in order to use PINOCCHIO outputs as GAEA inputs, it is necessary to adapt the merger trees to a different format, and add quantities that are used by GAEA and not available in PINOCCHIO as detailed in the following.

As a first step, for the existing haloes, at any given time we linearly interpolate in redshift the position, velocity, and mass between the two closest PINOCCHIO catalogues. In fact, both PINOCCHIO and GAEA do not require running on a shared, pre-defined time grid. Depending on the specific scientific application, without re-running PINOCCHIO we can interpolate the physical quantities available in the catalogues according to any given snapshot list. The accuracy of such interpolation is assured by the fact that PINOCCHIO halo positions are predicted with LPT. This allows us to run PINOCCHIO once and then freely choose the snapshot list as input to GAEA afterwards. For the purpose of this study, given the relatively small volume, we set twice as many snapshots as in the Millennium, equally spaced in the logarithm of the scale factor a from redshift 127 to 0. This guarantees the self-consistency with the GAEA predictions based on the Millennium merger trees and to concurrently increase the time sampling for a better time resolution. At redshifts above ~ 4 we also test a time sampling with four times the number of snapshots with respect to the Millennium one and we verify that the predictions are stable and robust as one decreases the integration time-step in the semi-analytic model.

Secondly, one physical quantity required by GAEA, but unavailable in PINOCCHIO, is the maximum rotational velocity of the halo V_{max}. In dark matter N-body simulations this quantity is estimated as:

$$V_{max} = \max\left(\sqrt{\frac{GM(r)}{r}}\right). \qquad (7)$$

The radius r runs over all the particles bound to the halo. In PINOCCHIO merger trees, such information is not directly available. We utilize instead:

$$V_{max} = f(z)V_{circ}, \qquad (8)$$

where a dimensionless factor $f(z)$ (of the order of unity), which is a function of redshift, multiplies the circular velocity of the halo which can be estimated as:

$$V_{circ} = \sqrt[3]{10GH(z)M}, \qquad (9)$$

where $H(z)$ is the Hubble parameter and M the mass of the halo defined and calibrated against FoF halo masses (Monaco et al. 2002).

Finally, it is important to note that in PINOCCHIO, when two haloes merge (referred to as the *accretion* time), the smaller one gives its mass to the larger one, and is *removed* from the halo list, meaning that it is not further updated. This means we cannot keep track of these haloes in the simulation once they become subhaloes. Therefore, we model the presence of subhaloes by assigning a survival time to each halo that is lost following a merger. This approach integrates the merger tree with information on its subhalo, as detailed by Berner et al. (2022) (see the next section).

2.3.1 Modelling subhaloes

In order to cast the above requirements into the PINOCCHIO-based approach, we have written a *translation* code that models the presence of subhaloes and adds physical information to properly mimic and output Millennium-like DMH merger trees. We use results derived from both theoretically and numerically predicted quantities to fill the required physical information and add the treatment of subhaloes.

In particular, we assign a population of subhaloes within each halo by: (1) assuming a spatial distribution for subhaloes following a Navarro–Frenk–White (NFW) density profile (Navarro, Frenk & White 1997); (2) implementing a statistically derived distribution for the angular momentum of subhaloes based on the orbital binding energies observed in numerical simulations (Zentner et al. 2005; Birrer et al. 2014); and (3) assigning a subhalo survival time since accretion (Boylan-Kolchin, Ma & Quataert 2008; Berner et al. 2022). Note that the NFW profile is not accurate for subhaloes in the inner regions of the DMHs, but describes well the observed spatial distribution of galaxies (e.g. Gao et al. 2004). We opt to sample the position of subhaloes from the NFW distribution at each output time, which means there is no correlation in their spatial position between two consecutive snapshots. In fact, subhalo orbits and positions do not affect the physical treatment of galaxies in the F20 version of the GAEA model.

We define a total merging time of each subhalo since the merging of the two haloes (accretion time) as the sum of the survival time of dark matter subhaloes, derived from simulations, and the residual merging time of their galaxies at the time subhaloes disappear. This is supported by the fact that in our runs of GAEA, satellite and orphan galaxies are equally treated. Our approach takes into account the two phases separately. We initially adopt a halo survival time to shape the first part of the total merging time, practically mimicking the satellite phase t_{sat}. Given the merging subhalo mass m_{sub}, the main halo mass M_{main} and the orbital circularity η at merger, we assume [with reference to equation (2.6) from Berner et al. 2022]:

$$t_{\mathrm{sat}} = A(D)\tau_{\mathrm{dyn}} \frac{\left(\frac{M_{\mathrm{main}}}{m_{\mathrm{sub}}}\right)^{b(D)}}{\log\left(1 + \frac{M_{\mathrm{main}}}{m_{\mathrm{sub}}}\right)} \exp(c\eta), \tag{10}$$

where A and b are functions of the linear growth factor $D(z)$ and c is a free parameter. The time-scale τ_{dyn} is the dynamical time at the virial radius, which is assumed to depend on the Hubble constant H only and its value is of the order of $\sim 0.1H^{-1}$.

Next, we add a second time calibrated by estimating the residual merging time of orphan galaxies assigned by GAEA as a function of the halo masses at the time the subhaloes disappear in the Millennium simulation. This was originally derived from the classical dynamical friction time-scale (Chandrasekhar 1943; Binney & Tremaine 1987), adapted to be applied in SAMs (e.g. De Lucia & Blaizot 2007; Boylan-Kolchin et al. 2008; De Lucia et al. 2010), which requires inputs of the position of the subhalo at the time it is lost in the simulation. Since this information is not available in PINOCCHIO, we assume a dependence only on the mass ratio between the merging halo (m_{sub}) and the main halo (M_{main}) at the accretion time. We also attempt to factor out the dependence on the redshift by directly fitting the ratio between the extra orphan time t_{orph} and the age of the Universe, t_{age}, at the accretion time. Based on the above considerations, we derive a formula for the orphan time, given by:

$$t_{\mathrm{orph}} = t_{\mathrm{age}}k \frac{\left(\frac{m_{\mathrm{sub}}}{M_{\mathrm{main}}}\right)^{\alpha}}{\log\left(1 + \frac{m_{\mathrm{sub}}}{M_{\mathrm{main}}}\right)^{\beta}}, \tag{11}$$

where k, α, and β are free parameters (see the next section for the calibrated values).

Finally, the total merging time of the satellite galaxy is the sum of the estimated halo survival time as in equation (10) and the modelled extra time for orphan galaxies given by equation (11) (see Appendix A). Note that while the individual contributions from these time-scales vary depending on the mass resolution of the DMH
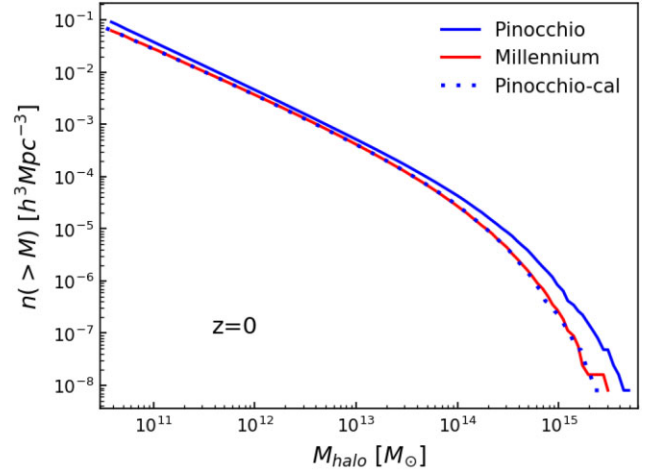
Figure 1. Halo mass functions (HMF) at redshift $z = 0$ from the PINOCCHIO Millennium-like box and the Millennium simulation (solid lines). Due to the different definition of the halo mass, at $z = 0$ the halo masses in PINOCCHIO are moderately higher compared to the Millennium haloes. We calibrate the PINOCCHIO HMF by using a polynomial fit of mass difference at a given number density that is a function of the redshift (dotted line).

trees, their combined total remains resolution-independent. This is because the total merging time is determined by the halo mass ratio and the accretion redshift. Hence, directly adding the total merging time to newly identified subhaloes ensures that the construction of the PINOCCHIO merger trees does not depend on the DM mass resolution.

2.4 Calibrating the trees

As discussed in Section 2.3, our reference GAEA realization is run on merger trees extracted from the Millennium Simulation. This is a numerical realization of a cosmological volume of side 500 h^{-1}Mpc assuming the WMAP1 lambda cold dark matter cosmology ($\Omega_{\Lambda} = 0.75$, $\Omega_m = 0.25$, $\Omega_b = 0.045$, $n = 1$, $\sigma_8 = 0.9$, and $H_0 = 73$ km s^{-1} Mpc^{-1}; Springel et al. 2005). We run a PINOCCHIO box that matches the Millennium one in terms of particle mass resolution, volume, and cosmological parameters. This run has been used to calibrate the time-scales discussed in the previous section.

The different definition of halo mass between the two simulations results in DM halo masses which are on average a factor of ~ 2–3 more massive in PINOCCHIO with respect to the Millennium (see Fig. 1). This difference requires us to calibrate, at each snapshot, the PINOCCHIO halo mass function (HMF) to match the Millennium one. To do so, we bin the range of cumulative number density n between the maximum halo mass for which we count at least ten objects and the minimum halo mass corresponding to the resolution of the simulation ($\sim 5 \times 10^8$ M$_{\odot}$). In such an interval, we fit both the PINOCCHIO and Millennium HMFs and we retrieve their ratio in halo mass for any given number density. Then, we multiply the PINOCCHIO halo mass by the correspondent correction factor. This operation provides haloes with the same mass distribution of the Millennium simulation, thus avoiding introducing systematic bias in subsequent steps. With a similar strategy, we calibrate the distribution of the maximum rotational velocity of the halo, V_{max}, introducing a correction factor in order to match the distribution extracted from the Millennium main haloes as a function of redshift (see equation 8). Additionally, the process of the assembly of the merger trees involves parameters we need to adjust, specifically the ones associated with the estimate of the merging time. For this scope, we run the GAEA

semi-analytic model on the *translated* merger trees generated from the PINOCCHIO box as described above. Then we aim at calibrating the parameters involved in the construction of the merging times t_{sat} and t_{orph} by reproducing the GSMF at redshift $z = 0$. In fact, the merging history of galaxies plays a crucial role in the build-up of their stellar and gas mass content, as well as shaping the cosmic star formation rate density and AGN activity across the age of the Universe.

We explore different combinations of the satellite t_{sat} and orphan t_{orph} time-scales in order to reproduce the normalization and the position of the knee of the GSMF at $z \sim 0$. In particular the total merging time of the satellite galaxies impacts on the total number density in terms of their relative contribution to the GSMF. Therefore, we calibrate the parameters in equations (10) and (11) by matching at the same time the GSMF of central and satellite galaxies obtaining the following values:

$$A = \begin{cases} 0.39 & \text{for } D(z) > 0.8 \\ 0.195 + \frac{0.195}{0.2}(D(z) - 0.6) & \text{for } 0.8 \geq D(z) \geq 0.6 \\ 0.195 \left(\frac{D(z)}{0.6}\right)^2 & \text{for } D(z) < 0.6 \end{cases}$$

$$b = 1.015 \cdot D(z)$$
$$c = 1.3$$
$$k = 0.3 \qquad\qquad (12)$$
$$\alpha = 0.94$$
$$\beta = 1.7.$$

Fig. 2 shows the result of our best estimate of the GSMF from both populations of galaxies (upper panel). The GSMF of centrals using the PINOCCHIO merger trees agrees well with the Millennium-based predictions for stellar masses above few times $10^{10}\,\mathrm{M_\odot}$, throughout the knee until the exponential cut-off at the high-mass end. On the other hand, satellites show a substantial difference (a factor of up to ~ 4) at the low mass end of the GSMF, i.e. at masses below $\sim 10^{10}\,\mathrm{M_\odot}$, even though the total gap in the bottom panel is dominated by the central galaxies. We argue that this difference is due to the intrinsic differences in the features of the PINOCCHIO and Millennium simulations in the definition and construction of merger events (orbit crossing versus FoF). As a consequence, this effect causes a dearth of small mass haloes as one approaches $\sim$ few $10^9\,\mathrm{M_\odot}$, explaining the gap in the number density of galaxies. However, if one compares the total GSMF combining all types of galaxies (bottom panel), the difference in the low-mass end reduces to a factor of ~ 2 or less. We also verify that at earlier epochs, when the fraction of satellite galaxies is lower, the impact of the merging time is marginal. Our GSMF reproduces the trend obtained from the Millennium-based predictions with a better agreement compared to $z \sim 0$. Bearing in mind these caveats, we consider the calibration resulting in the GSMF depicted in Fig. 2 as being sufficiently accurate for the scope of this work and we opt not to calibrate the GAEA physical parameters keeping the values proposed by F20 (see also Appendix B).

2.5 Seeding SMBHs

The primary goal of our paper is to investigate the impact of the Pop III.1 SMBH seeding scheme on galaxy and SMBH properties. This seeding scheme is illustrated in Fig. 3 (for a more detailed introduction of the seeding we refer to Banik et al. 2019; Singh et al. 2023). In the figure, three stars, denoted as A, B, and C, reside in different haloes. Among them, only A and C evolve into Pop III.1 supermassive protostars, while B is designated as a lower mass Pop
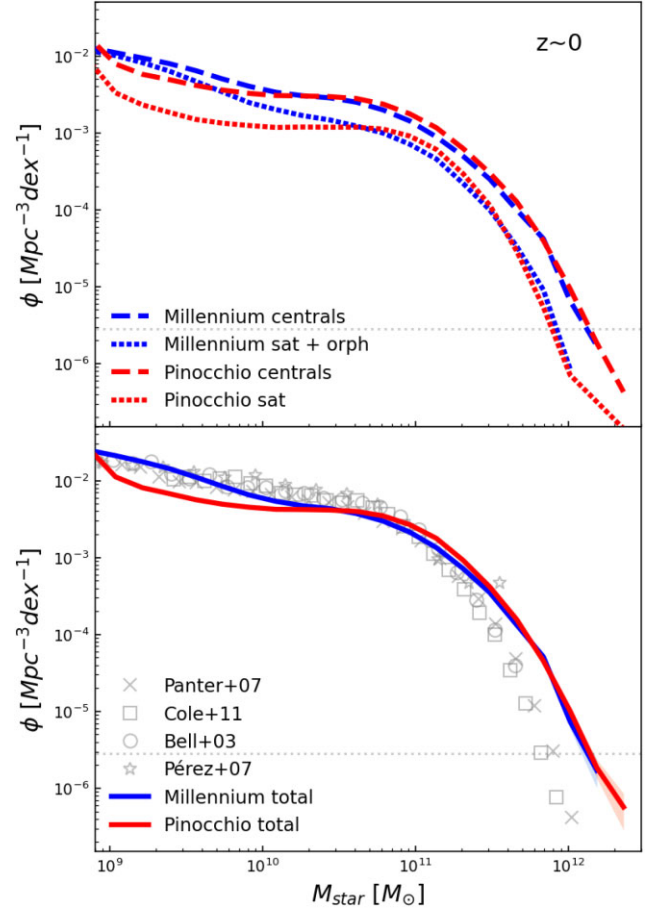

Figure 2. *Upper panel:* GSMF at redshift z = 0 from the Millennium-like box. Dashed (dotted) lines indicate the contribution of the central (satellite and orphan) galaxies, respectively. While central galaxies show remarkable agreement, PINOCCHIO's low mass satellites differ by a factor of ~ 4 in number density with respect to the Millennium ones. *Lower panel:* Total GSMF at $z = 0$ from the Millennium-like box. The symbols show observed data points from Cole et al. (2001), Bell et al. (2003), Panter et al. (2007), and Pérez-González et al. (2008). This plot shows the goodness of the calibration, especially above $10^{10}\,\mathrm{M_\odot}$.
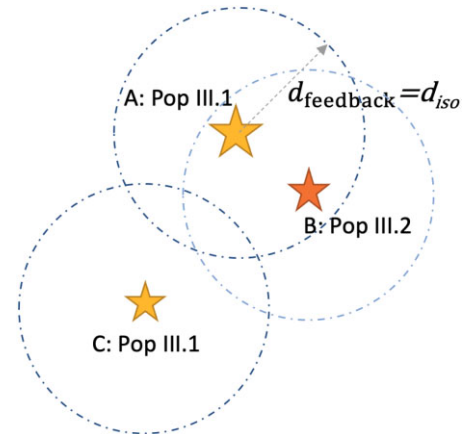

Figure 3. A simplified illustration of the Pop III.1 SMBH seeding scheme (see the text) showing the conditions for a star to be isolated enough to be considered as a Pop III.1 star. Adapted from Singh et al. (2023).

III.2 star. This classification depends on their physical separation from other sources at the time of their formation.

Star A, forming first, exerts its influence within a sphere of radius equal to $d_{feedback}$, primarily driven by radiative feedback. Since this star originates in a pristine primordial gas environment, devoid of any influence from neighbouring stars, it falls under the category of a Pop III.1 star. Star B, on the other hand, forms at a distance less than $d_{feedback}$ from star A, subjecting it to the effects of feedback. Consequently, it is classified as a Pop III.2 star (or even a Pop II star if the gas cloud it forms from is chemically enriched). Finally, star C forms beyond the regions influenced by feedback from stars A and B. As a result, it is are designated as another Pop III.1 source.

The physical mechanism that may allow SMBH formation is the impact of dark matter annihilation heating on the structure of the Pop III.1 protostar (Spolyar et al. 2008; Natarajan et al. 2009; Rindler-Daller et al. 2015). The expected effect is to keep the protostar relatively large and cool, thus emitting a weak flux of ionizing radiation. Efficient collapse of the baryonic content of the minihalo to the Pop III.1 protostar, i.e. yielding a mass of $\sim 10^5 \, M_\odot$, is assumed to occur. After a few Myr of evolution, this source is then expected to form a SMBH of similar mass. Thus the initial mass of the SMBH seeds that we implement in the Pop III.1 scheme is $M_{BH} = 10^5 \, M_\odot$.

The main parameter of the Pop III.1 model is the isolation distance, d_{iso}, which is required for a minihalo to form a Pop III.1 source. Banik et al. (2019) and Singh et al. (2023) have shown that values of $d_{iso} \simeq$ 50 to 100 kpc (proper distance) are sufficient to yield overall numbers of SMBHs consistent with estimates of local number densities at $z = 0$. We will thus consider values of $d_{iso} = 50, 75, 100$ kpc in our modelling.

We also consider two other seeding models. The first of these is the BH seeding scheme that is implemented within GAEA and described in detail in Xie et al. (2017). Recall that this scheme has been tested at the Millennium simulation resolution and is intended to be a subgrid model that is not attempting to mimic any seeding scenario. Whenever a new DMH is resolved in the PINOCCHIO simulation, we assign it a BH mass (M_{BH}) scaled with the parent DMH mass (M_{DM}):

$$M_{BH} = \left(\frac{M_{DM}}{10^{10} \, M_\odot h^{-1}} \right)^{1.33} \frac{10^{10} \, M_\odot h^{-1}}{3 \times 10^6}, \tag{13}$$

where the index of the relation is derived from Volonteri, Natarajan & Gültekin (2011). We refer to this scheme in which all haloes are seeded as ALS (All Light Seed). Note that this is an ad-hoc model that mimics the formation of seeds from Pop III stars and estimates their evolution by accretion before the halo is resolved. Given the relatively high mass resolution of our PINOCCHIO box (see Section 2.1), applying equation (13) to the M_{DM} mass distribution results in BH seed masses of the order of $\sim 10^{1-2} \, M_\odot$. This mechanism effectively depicts a scenario where every single halo is seeded with a Pop III remnant BH and can be considered an implementation of the standard light-seed Pop III model described in Section 1. Note that this seeding scheme has been tested previously only at the resolution of the order of the Millennium Simulation (Xie et al. 2017). The GAEA version presented in F20 and used in the model calibration described in Section 2.4 is based on this latter seeding scheme.

Finally, for continuity with Paper II we also consider the HMT seeding scheme, where all haloes with mass $> M_{thr} = 7.1 \times 10^{10} \, M_\odot$ are seeded with a $1.4 \times 10^5 \, M_\odot$ BH. This is the typical seeding scheme used in hydro simulations (e.g. Vogelsberger et al. 2014), however the value of the threshold mass is determined by the mass resolution of simulations able to resolve galaxies in a cosmological box. The box used to obtain our results has a much higher resolution, so this scheme can be considered as a toy model

for a seeding scheme where BH seeds appear later in the evolution of the Universe.

3 RESULTS

Here we present the predicted properties of the galaxy populations based on DMH merger trees extracted from the 40 Mpc h^{-1} PINOCCHIO box described in Section 2.1 and *translated* as explained in Section 2.3. We evaluate the Pop III.1 seeding model for three cases of $d_{iso} = 50, 75$, and 100 kpc (see Section 2.5), as well as for the ALS and HMT seeding schemes. Unless otherwise specified, we apply the accretion scheme onto the SMBH described in Section 2.2.1. Throughout this work, the three cases of isolation distance $d_{iso} = 50, 75$, and 100 kpc are depicted in orange, red, and blue, respectively, while the ALS and HMT models are shown in magenta and green, respectively.

3.1 Occupation fractions

We examine the cosmic evolution of the fraction of galaxies that are seeded with SMBHs, i.e. the *SMBH occupation fraction*, including as a function of various physical properties. In Fig. 4 we show the evolution of the SMBH occupation fraction, i.e. the fraction of seeded galaxies, as a function of various galaxy properties from redshift $z \sim 10$ down to $z \sim 0$. Different columns indicate different galaxy quantities, from left to right: halo mass, stellar mass, hot gas mass, and star formation rate (SFR). The ALS seeding scheme is by construction always identical to unity. For a more meaningful comparison in terms of occupation fractions of SMBHs, here we also consider the ALS case applying a cut in BH mass above $10^5 \, M_\odot$ (hereafter depicted with the label ALS-cut).

At all epochs, the SMBH occupation fractions as a function of halo mass, stellar mass, and hot gas mass have similar behaviours across Pop III.1 seeding models. As the isolation distance decreases, the occupation fraction rises. SMBHs tend to reside in the more massive systems, as the Pop III.1 model places them in the first locally formed mini-haloes, which are more likely to be the progenitors of the largest structures later on. While the high-mass end occupation fraction as a function of halo mass reaches unity for all models at redshift zero, this is not the case for the occupation fraction as a function of stellar mass, i.e. only ~ 60 per cent of galaxies with highest level of stellar mass ($\sim 10^{12} \, M_\odot$) are seeded in the $d_{iso} = 100$ kpc case, but rising to about 100 per cent in the $d_{iso} = 50$ kpc case. The various Pop III.1 cases show occupation fractions that rise gradually for $M_{star} \gtrsim 10^7 \, M_\odot$ to $10^9 \, M_\odot$ as d_{iso} rises from 50 to 100 kpc. On the other hand, the HMT model shows an occupation fraction that rises very steeply to unity for stellar masses $\gtrsim$ few $\times 10^9 \, M_\odot$ across all epochs. The ALS-cut case presents a similar shape, but shifted downward by one order of magnitude to $10^8 \, M_\odot$ by $z \sim 0$. This reflects the fact that, when a low mass seeding scenario is applied, the viscous accretion mode soon establishes a BH growth rate proportional to the SFR reproducing the local scaling at the latest epochs ($M_{star} \sim 10^3 M_{BH}$). Therefore, applying a cut in M_{BH} corresponds to impose a sharp threshold for M_{star}.

Thus a key difference between the Pop III.1 models and the HMT and ALS seeding schemes is that the Pop III.1 models have much smaller SMBH occupation fractions at relatively high values of M_{star}. This implies a population of unseeded galaxies reaching large values of M_{star}. Indeed, in the absence of AGN feedback, these systems keep forming stars with relatively high rates at all redshifts, which influences the SMBH occupation fraction versus SFR, discussed
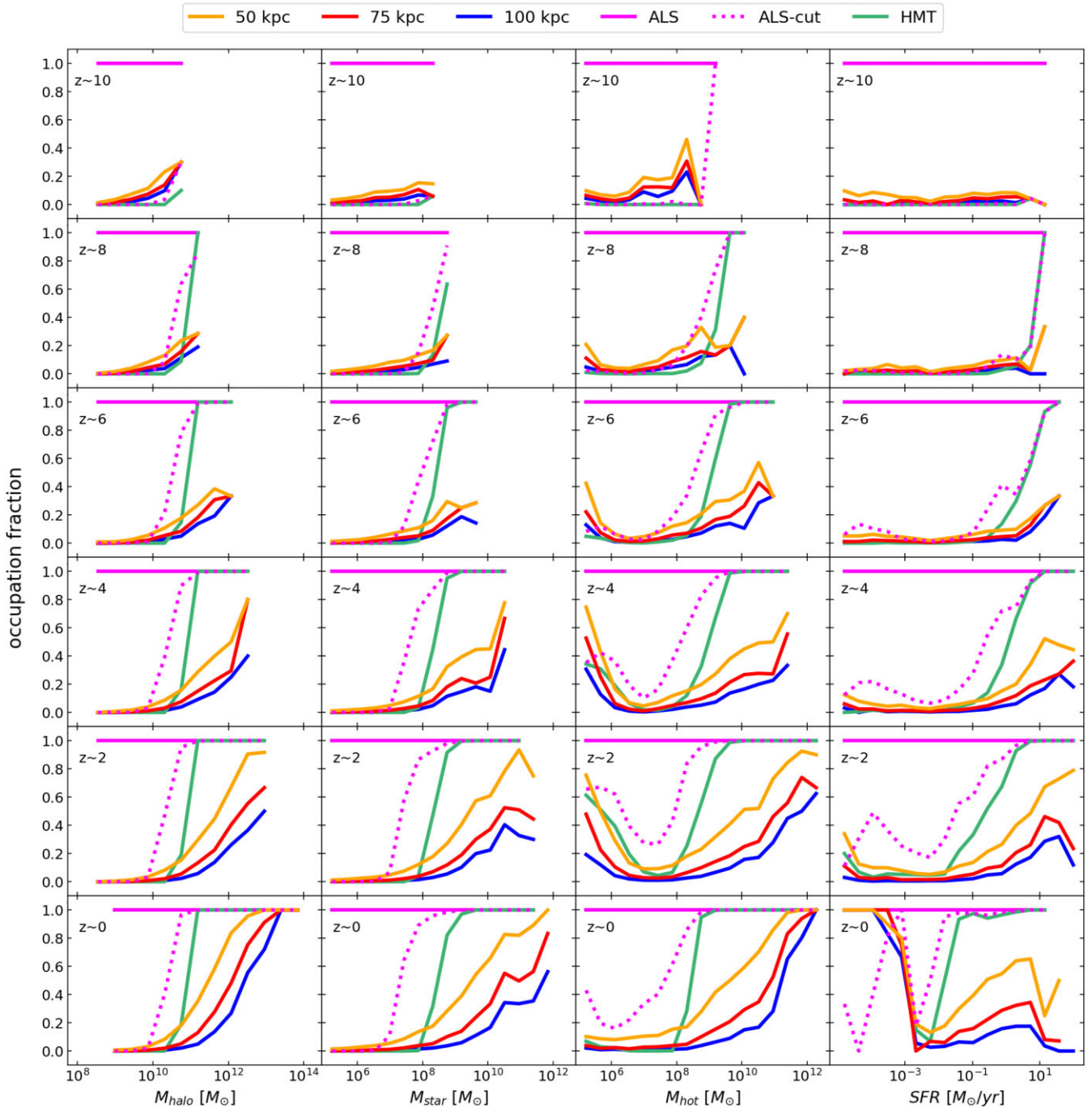
Figure 4. Occupation fraction of seeded galaxies as a function of different galaxy properties for several redshifts. From left to right: halo mass, stellar mass, hot gas mass, and star formation rate (SFR). The six lines show different seeding mechanisms.

below. A related consequence is that the Pop III.1 models have a larger scatter in the $M_{star} - M_{halo}$ relation, discussed in Section 3.4.

When considering SMBH occupation fraction as a function of hot gas mass, to the extent that more massive haloes and/or stellar components correlate with M_{hot}, we see similar trends. However, at intermediate redshifts we see that there is a population of seeded galaxies with very low values of M_{hot}, which are attributed to systems in which AGN feedback prevents the build up of hot gas mass.

Fig. 4 also shows the evolution of the occupation fractions as a function of SFR. At later epochs, from redshift ~ 4 down to

intermediate redshifts (z∼2), one sees how seeded galaxies, mostly residing in more massive galaxies, tend to have larger SFR. At the same time AGN feedback begins to influence the gas in these galaxies, leading to an efficient suppression of star formation in massive systems. This demonstrates the effectiveness of radiomode AGN feedback in keeping galaxies passive. By redshift z∼0 the fraction of passive galaxies, characterized by SFRs lower than 10^{-3} M$_\odot$ yr^{-1}, reaches SMBH occupation fractions of unity across all models. However, we see that the ALS-cut scheme reaches one about SFR of 10^{-3} M$_\odot$ yr^{-1}, but it drops down to small fractions soon after. One
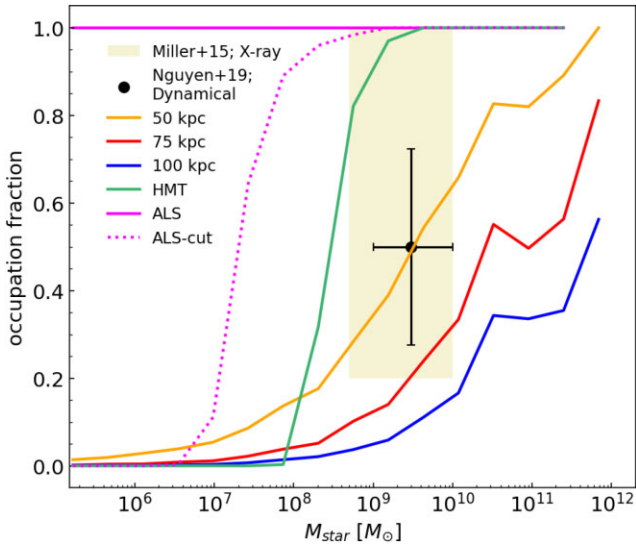
Figure 5. Occupation fraction of seeded galaxies as a function of the stellar mass at redshift zero. The six lines show different seeding mechanisms. In the range of stellar masses between few in 10^8 and $10^{10}\,M_\odot$, we compare against different observational constraints for the occupation fraction. X-ray sources detected in local surveys pose some lower limit to the occupation fraction as presented by Miller et al. (2015) drawn as the shaded region. We also show the more stringent constraints as reported by Nguyen et al. (2019) obtained from dynamical findings in a small sample of nearby galaxies.

should keep in mind that ALS-cut does not track the whole population of seeded galaxies, but only the ones having $M_{BH} > 10^5\,M_\odot$. As opposed to the other models, this latter subsample of galaxies is not exclusive in terms of radiomode AGN feedback since this also affects galaxies with BHs just below the BH mass cut, contaminating the measurements of the occupation fraction for the SFR as well as for the hot gas.

As a point of comparison with observational data, in Fig. 5 we illustrate constraints for the fraction of observed local galaxies hosting a SMBH in the range of stellar masses between few in 10^8 and $10^{10}\,M_\odot$. Observationally, dynamical and X-ray measurements based on local galaxies seem to agree that at least $\gtrsim 50$ per cent of the population in this mass range host a SMBH with mass $\sim 10^{4-6}\,M_\odot$ (see discussion in Greene et al. 2020). In particular, Nguyen et al. (2019) show that out of 10 galaxies within a distance of 4 Mpc for which dynamical measurements are available, only five SMBHs are detected, inferring a lower limit for the occupation fraction. Additionally, Miller et al. (2015) advocate a lower limit of 20 per cent with a most probable estimate of around 70 per cent based on the detection of X-ray sources in local galaxies within a comparable stellar mass.

Fig. 5 illustrates that current observational measurements are not of sufficient precision to discriminate between the different models. If the quality and statistics of observational samples can be increased to reduce the uncertainties, then the presented models could be distinguished. However, it is interesting to note that our simulations present a better agreement in terms of the occupation fraction when d_{iso} approaches the value of 50 kpc, as we allow more haloes to be seeded. Conversely, the 75 and 100 kpc cases struggle to produce large enough occupation fractions while the ALS-cut and HMT model tends to create more numerous SMBHs although still in agreement with Miller et al. (2015). On the other hand, the ALS scenario would be difficult to test against current observations as the

totality of galaxies in this mass range would host a BH, whose mass would span from stellar seeds up to the SMBH regime.

3.2 Stellar mass function

In Fig. 6 we illustrate the cosmic evolution of the GSMFs evaluated for the Pop III.1 seeding models from $z \sim 0$ up to 3. For the redshift zero case, we see that below stellar masses of approximately $3 \times 10^{10}\,M_\odot$ the predicted functions match reasonably well down to low masses of $M_{star} \sim 10^8\,M_\odot$. In this regime, the majority of galaxies are non-seeded, and so there is little impact, i.e. due to AGN feedback, of varying d_{iso}. On the other hand, reducing d_{iso} from 100 to 50 kpc has a dramatic impact at the high-mass end of the GSMF. Specifically, while the 75 and 100 kpc models struggle to reproduce the exponential cutoff of the GSMF above a few $\times 10^{10}\,M_\odot$, the 50 kpc case is able to maintain good agreement with the observational data. This is due to the action of AGN feedback in suppressing the build-up of high stellar mass galaxies. We see that the ALS and HMT models, having similar, saturated occupation fractions at high stellar masses, are also able to reproduce the local high-mass end of the GSMF. It is worth stressing that the agreement with observational constraints cannot be improved by a different parameter calibration, as the lack of a central SMBH in unseeded galaxies prevents the onset of Radio-mode feedback in the first place, and stellar feedback alone is insufficient to reduce the number of massive galaxies while keeping a good agreement at lower masses and using realistic loading factors (White & Frenk 1991).

Moving to higher redshifts, the differences between seeded and non-seeded galaxies become less visible in terms of average stellar mass distribution, as the SMBH are not big enough to affect the evolution of the host galaxy by means of radio-mode feedback. This also reflects in the GSMF: if we look at the evolution of the GSMF up to redshift $z \gtrsim 2$ right at the peak of the cosmic SFR, the different isolation distance scenarios become more similar and all of them tend to agree with the observed data (see higher redshift panels). This makes it more difficult to use such an observable to discern among the seeding criteria, i.e. d_{iso}, at $z \gtrsim 1$.

3.3 Local black hole mass function

Here we present basic predictions for the mass distribution of the SMBH population at $z \sim 0$. As shown in Fig. 7, the three d_{iso} cases predict different trends for the black hole mass function (BHMF). As a reference, observational constraints are compared to our predictions, derived from a sample of local galaxies (shaded area Mutlu-Pakdil, Seigar & Davis 2016) and from the unbiased corrected relation from Shankar et al. (2020) (hatched area). Overall, we see that the $d_{iso} = 75$ kpc case predicts number densities of SMBHs in approximate agreement with the observational data. The $d_{iso} = 100$ kpc case falls slightly below the observed values, while the $d_{iso} = 50$ kpc case is slightly higher.

In the high mass end, we see that both the HMT and ALS models do not produce as many very high mass SMBHs as the Pop III.1 models. We expect this is due to a combination of factors: (1) competition between SMBHs for available gas mass; (2) a greater degree of AGN radiomode feedback, due to larger occupation fractions, which reduces the amount of gas available for SMBH accretion. Conversely, the HMT and ALS models predict the presence of much larger populations of lower mass SMBHs. In particular, the ALS model, which invokes seeds down to stellar mass scales, predicts a large population of IMBHs.
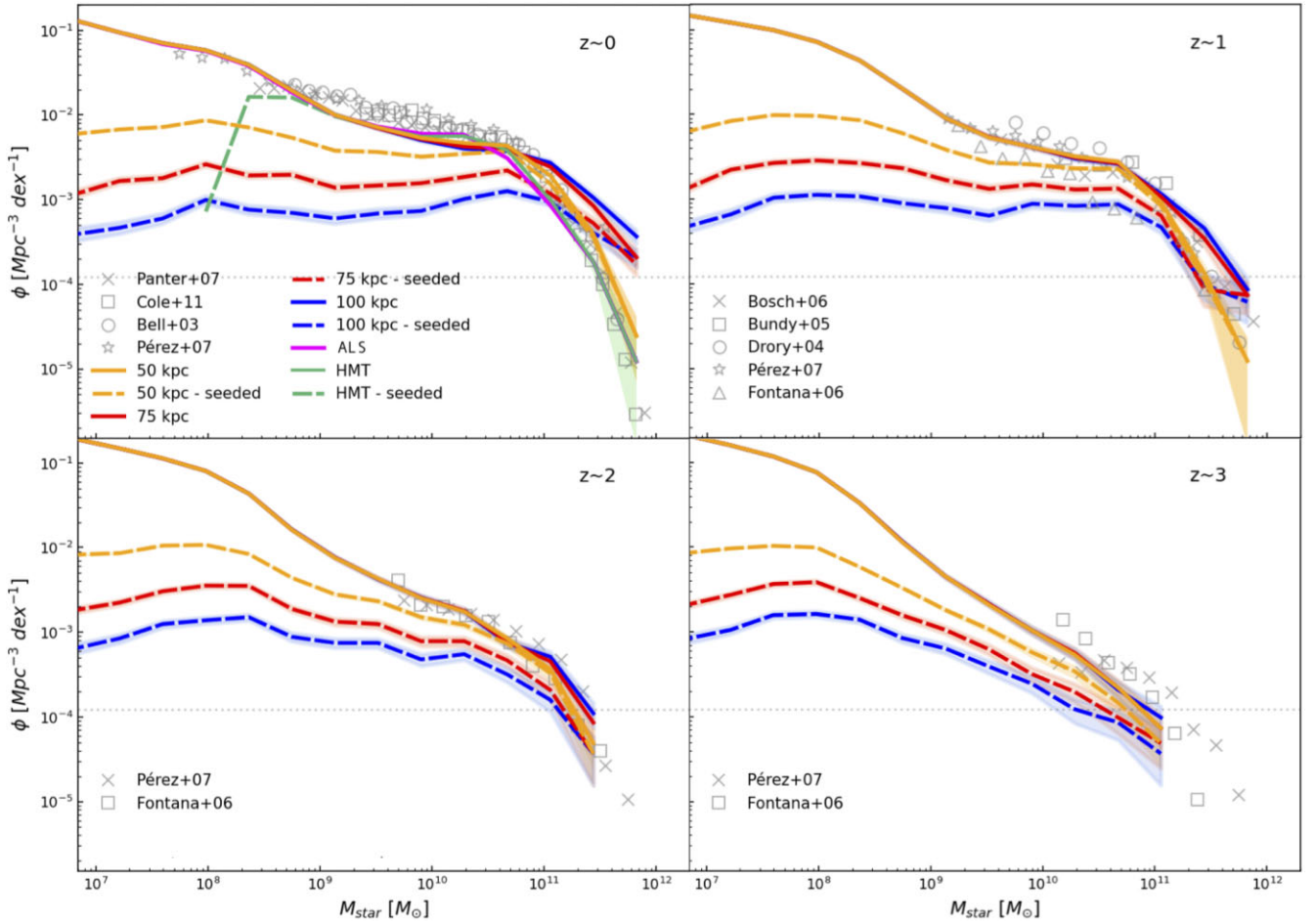
Figure 6. Cosmic evolution of the GSMF from redshift 0 up to 3. Solid (dashed) lines indicate the contribution of all (seeded) galaxies, respectively. The shaded areas depict the Poisson uncertainties in each mass bin. Results for Pop III.1 models with three values of isolation distance (in proper distance) are shown, as labelled. Observed data are in grey symbols (Cole et al. 2001; Bell et al. 2003; Drory et al. 2004; Bundy, Ellis & Conselice 2005; Fontana et al. 2006; Panter et al. 2007; Pérez-González et al. 2008; Van Den Bosch et al. 2008). As a reference, the dotted horizontal line stands for 10 objects per mass bin in the whole volume of the box. The GSMF tells us the isolation distance parameter that better reproduces the observed trend, especially at the massive end. The 50 kpc case agrees with the exponential cut off of the massive population of galaxies from the local relation, where almost every galaxy with a stellar mass higher than $\sim 3 \times 10^{10}\,\mathrm{M_\odot}$ is assumed to host a SMBH, up to $z \sim 1$. At redshift 0 we compare with the HMT and ALS seeding schemes. These two cases mostly overlap in the graph. While ALS well reproduces the local observational trend by construction, HMT naturally seeds every massive galaxy resulting in efficient quenching of star formation in such systems. We use them as reference models to validate the Pop III.1 seeding at redshift $z = 0$. The dashed line of the HMT scheme tells us that the fraction of seeded galaxies rises sharply up to one above $\sim 10^9\,\mathrm{M_\odot}$ as shown from Fig. 5.

3.4 The $M_{\mathrm{BH}} - M_{\mathrm{star}}$ relation

Here we consider the relation between central SMBH mass and galactic stellar mass for the different models of SMBH seeding. Recall that, as described above, these results are based on the fiducial SMBH growth model adopted by F20. The scatter plots in Fig. 8 show the populations of seeded galaxies for the various seeding schemes (columns) at redshift zero (bottom row), with high redshift results shown in the other rows. Note that in the following analysis, we exclude unseeded galaxies, which, as discussed in Section 3.1, for the Pop III.1 models can be a significant fraction of the systems even in the high M_{star} regime. Thus when comparing our results to observational samples, only galaxies with confirmed SMBHs, i.e. not just upper limits, should be used.

3.4.1 Redshift zero results

Focusing first on the local results, we see a general trend of more massive black holes being found in galaxies with larger stellar

masses. Since the Pop III.1 model assumes seed masses of $10^5\,\mathrm{M_\odot}$, we see a flattening of the $M_{\mathrm{BH}} - M_{\mathrm{star}}$ relation to this level as one goes to lower mass galaxies. This feature is not seen in the HMT model since requiring a threshold halo mass of $7 \times 10^{10}\,\mathrm{M_\odot}$ naturally imposes an effective threshold on M_{star} for seeded galaxies. This feature is also not seen in the ALS seeding scheme, since the seed masses in this model are much smaller than $10^5\,\mathrm{M_\odot}$.

In general, the $M_{\mathrm{BH}} - M_{\mathrm{star}}$ relation can be approximated as a power law, especially if one restricts to limited ranges in stellar mass. We thus fit the following function to the distributions:

$$M_{\mathrm{BH}} = M_{\mathrm{BH},9} \left(\frac{M_{\mathrm{star}}}{10^9\,\mathrm{M_\odot}} \right)^\alpha \tag{14}$$

and consider a stellar mass of $10^9\,\mathrm{M_\odot}$ as fiducial scale at which to divide *low-mass* and *high-mass* galactic systems. However, we set a lower limit of $M_{\mathrm{star}} = 10^8\,\mathrm{M_\odot}$, which is designed to make the metrics of the low-mass case easier to compare to observed systems. We also consider a *very high-mass* range at $M_{\mathrm{star}} > 10^{11}\,\mathrm{M_\odot}$. We carry out
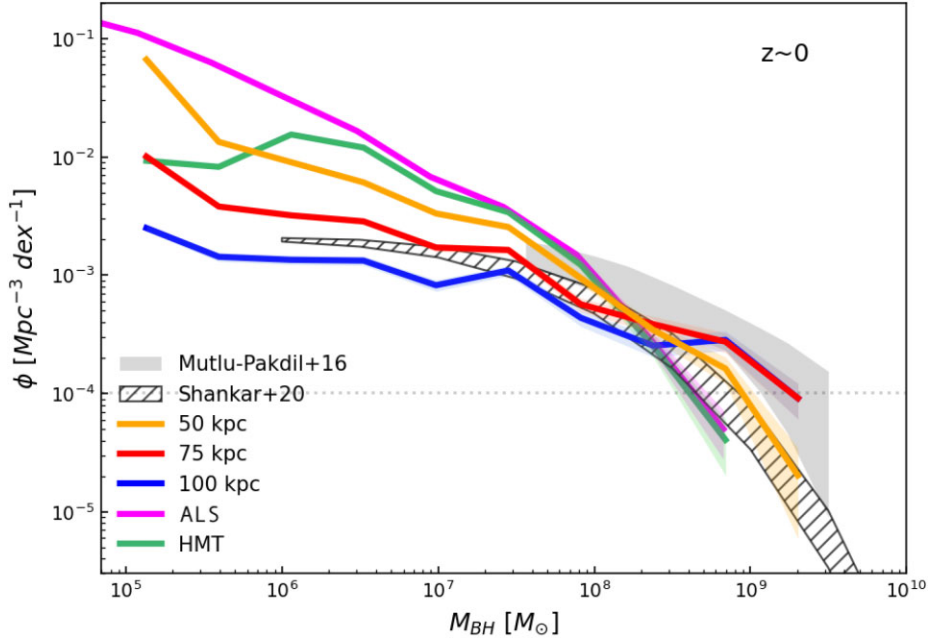
Figure 7. Black hole mass function at redshift $z \sim 0$. Solid lines indicate the contribution of different seeding schemes. The shaded areas around the lines depict the Poisson uncertainties in each mass bin. Observed data are taken from a sample of local galaxies (shaded area Mutlu-Pakdil et al. 2016) and from the unbiased corrected relation from Shankar et al. (2020) (hatched area). As a reference, the dotted horizontal line stands for 10 objects per mass bin in the whole volume of the box.

power-law fits to the binned median values of M_{BH}, i.e. giving equal weight to the different bins of M_{star}, which are distributed evenly in logarithm and spaced every ~ 0.33 dex. We require at least five sources in a given bin to include it in the fit. Every median value is then weighted with its corresponding standard error, which in the least populated high-mass bins is about 0.3 dex. We report the maximum range of the black hole distribution via a metric $\overline{M}_{BH,max10}$, which is the geometric mean mass of the ten most massive black holes in the simulation domain of $\sim (60 \text{ Mpc})^3$. We also measure the dispersion, σ about each best-fitting power-law $M_{BH} - M_{star}$ relation, averaging the dispersions in each mass bin equally. The redshift zero results for α, $M_{BH,9}$ and σ for the low-, high-, and very high-mass cases, as well as $\overline{M}_{BH,max10}$, are reported in Table 1 for the various seeding schemes. These power-law fits are also plotted in Fig. 9.

For galaxies with $M_{star} < 10^9 \text{ M}_\odot$, the properties of the best-fitting power law show that the Pop III.1 models have the most shallow power-law indices, i.e. $\alpha_{low} \simeq 0.6$, with the $d_{iso} = 100$ kpc case having the shallowest index of 0.56. In comparison, the HMT model has $\alpha_{low} \simeq 1.3$, while the ALS model has $\alpha_{low} \simeq 0.8$. On the other hand, the amplitude of the power-law fits, as measured by $M_{BH,9}$, show very little variation ($\lesssim 0.1$ dex) between the models. The dispersion about the power law is similar among the models at 0.5 dex, except for the two larger d_{iso} cases where it drops at 0.4 dex for the 100 kpc model. This trend in the Pop III.1 models results from the fact that for smaller values of d_{iso}, a broader variety of haloes is seeded, leading to a wider range of growth and star formation histories that then lead to greater scatter in the $M_{BH} - M_{star}$ relation.

In the high-mass regime, with $M_{star} > 10^9 \text{ M}_\odot$, the processes leading to black hole growth and star formation result in an $M_{BH} - M_{star}$ relation that is relatively similar between the different seeding schemes, so it becomes harder to distinguish the models from the statistics of their $M_{BH} - M_{star}$ relations. Nevertheless, from the results shown in Table 1 we notice that, in contrast to the low-mass

regime, the Pop III.1 models have systematically higher values of dispersion about their best-fitting power laws, i.e. $\sigma_{high} \simeq 0.7$, while the HMT model has $\sigma_{high} \simeq 0.5$ and the ALS model 0.4. Similar conclusions can be drawn for the very high-mass regime. This is caused by the Pop III.1 models having quite large volumes that are prevented from forming seeds, i.e. via the isolation distance criteria, and these volumes can contain relatively massive haloes that form galaxies with relatively high M_{star} that either never host a SMBH (see the comparatively low occupation fractions in Fig. 5 of the Pop III.1 models) or gain a relatively low-mass SMBH from later merger with a smaller halo/galaxy.

We also notice that at the highest masses there is evidence for steepening of the power-law behaviour of the $M_{BH} - M_{star}$ relation. This is most noticeable for the Pop III.1 models, which tend to have a greater number of more massive SMBHs (see Fig. 7). After inspecting the accretion histories of some example cases, we attribute this as being due to reduced impact of AGN feedback in the Pop III.1 models given their overall smaller numbers of SMBHs. Indeed, AGN feedback processes act as regulators of the cold gas content in galaxies, by heating their cold gas component and displacing it to the hot phase. This implies that unseeded galaxies in Pop III.1 models tend to accumulate larger cold gas reservoirs with respect to seeded ones. Therefore, when these galaxies became satellites in massive haloes and merge with a central seeded galaxies, they provide more cold gas available for accretion onto the central SMBH with respect to seeded galaxies (see Section 2.2.1), thus enhancing the final BH mass achieved compared to the HMT and ALS cases.

To quantify these differences, we refer to the power-law fits for the very high-mass regime (see Table 1). In the top panel of Fig. 9 we see that for larger values of d_{iso} Pop III.1 models show a steeper slope up to ~ 1.7 for the 100 and 75 kpc cases, while other seeding criteria present comparable shallower trends with power-law indexes about 1.3–1.4. This is a direct consequence of the already mentioned competition effect on the BH accretion (e.g. see also the BHMF in
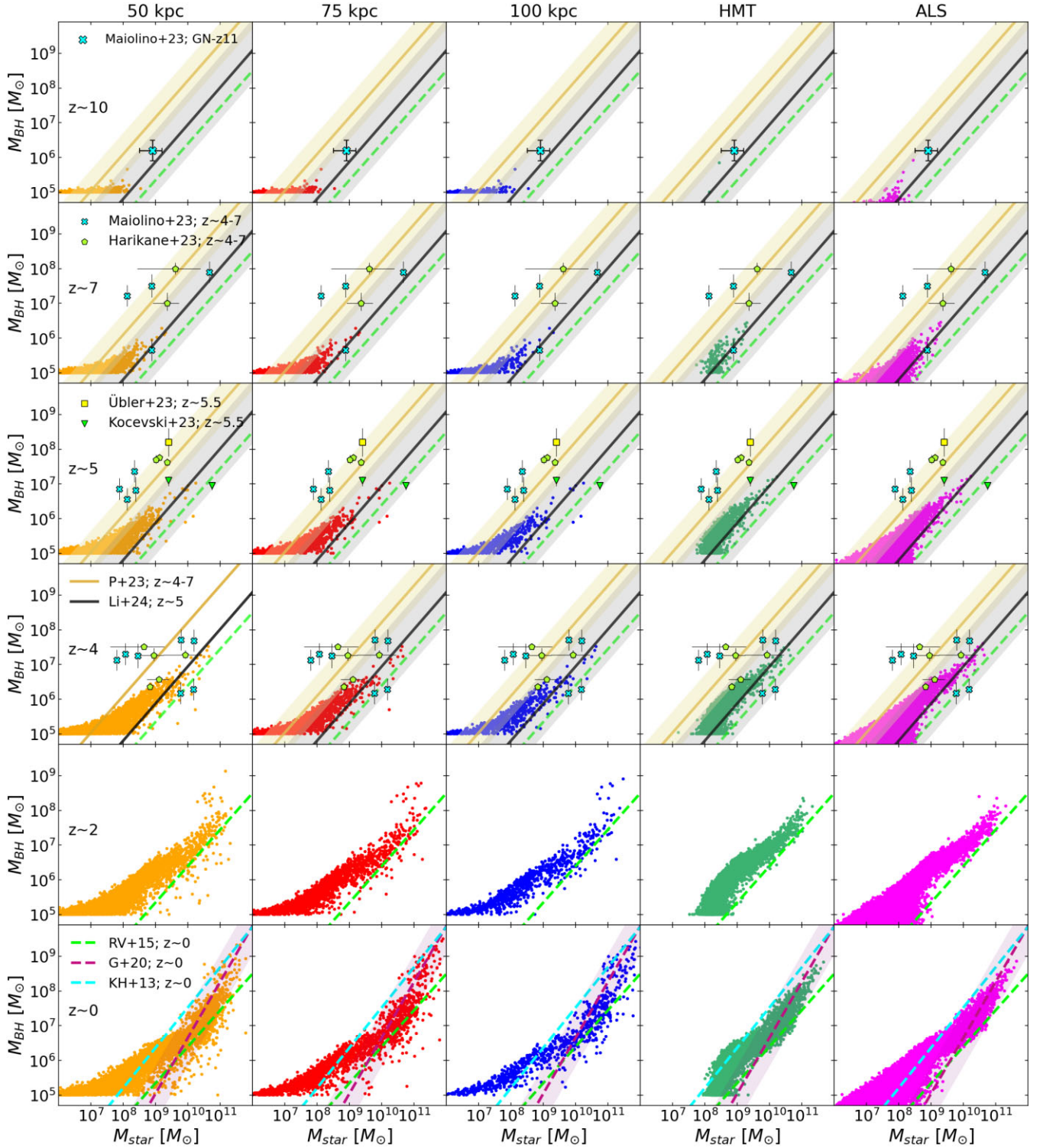
Figure 8. Scatter plot of the evolution of the $M_{\rm BH} - M_{\rm star}$ relation at several redshifts. Different columns represent various seeding schemes. At redshift $z \sim 0$ we compare our predictions for our seeded galaxies with several best fits from local observations: dynamical measurements from Kormendy & Ho (2013) (KH+13), including massive bulge-dominated quiescent galaxies, while Reines & Volonteri (2015) (RV+15) use a different mass-to-light ratio, plus an extended sample combining local early- and late-type galaxies by Greene et al. (2020) (G+20). At $z \sim 2$, we report the RV+15 fit for reference. Moving upward, the high-z rows show the comparison with recent results from the JFAINT sample: in Pacucci et al. (2023), they directly fit the data in the redshift range $z \sim 4 - 7$ while Li et al. (2024) estimate an unbiased fit taking into account the uncertainties on the mass measurements and selection effects. Shaded regions illustrate the intrinsic scatter at 1-sigma according to each relation. Coloured symbols show faint AGNs taken from Harikane et al. (2023), Kocevski et al. (2023), Maiolino et al. (2024), Übler et al. (2023) and reported according to their redshifts. In the top row, results at $z \sim 10$ are shown against the single data point (GN-z11) from Maiolino et al. (2024).

Table 1. Fitting parameters and derived quantities: the slope α, the intercept $M_{BH,9}$ (at $M_{star} = 10^9 M_\odot$), and dispersion σ are shown at z∼0. We also report the average (geometric mean) mass of the 10 most massive BHs.

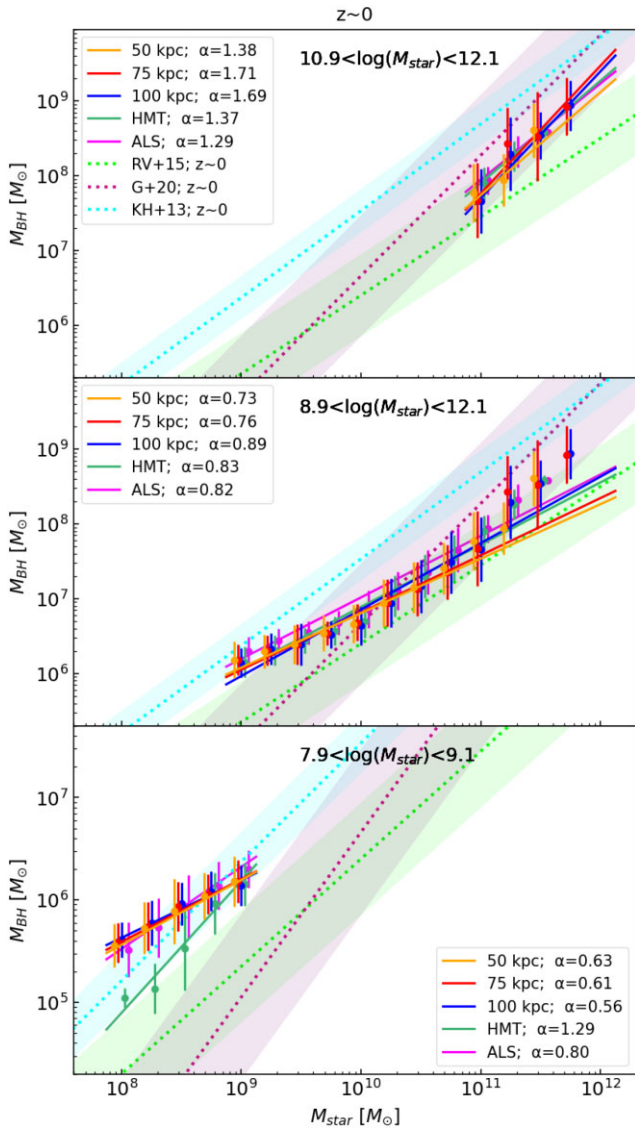| | z∼0 | | | | |
	50 kpc	**75 kpc**	**100 kpc**	**HMT**	**ALS**
α_{vh}	1.38	1.71	1.69	1.37	1.29
$\log(M_{BH,9,vh}[M_\odot])$	4.99	4.35	4.31	5.16	5.37
σ_{vh}[dex]	0.74	0.98	0.79	0.32	0.29
α_{high}	0.73	0.76	0.89	0.83	0.82
$\log(M_{BH,9,high}[M_\odot])$	6.08	6.05	5.97	6.06	6.19
σ_{high}[dex]	0.61	0.68	0.63	0.43	0.40
α_{low}	0.63	0.61	0.56	1.29	0.80
$\log(M_{BH,9,low}[M_\odot])$	6.19	6.20	6.19	6.18	6.32
σ_{low}[dex]	0.50	0.43	0.40	0.50	0.51
$\log(\overline{M}_{BH,max10}[M_\odot])$	8.99	9.26	9.23	8.62	8.65

Figure 9. Power-law fits to the $M_{BH} - M_{star}$ relation at $z \sim 0$. Dotted lines depict local fits with associated dispersion (shaded areas). The indices α are shown in the legend. Solid lines indicate the fit results to the median SMBH masses (data points with dispersion) in several stellar mass bins for different seeding models. The stellar mass range covered by the solid lines corresponds to the fitted interval.
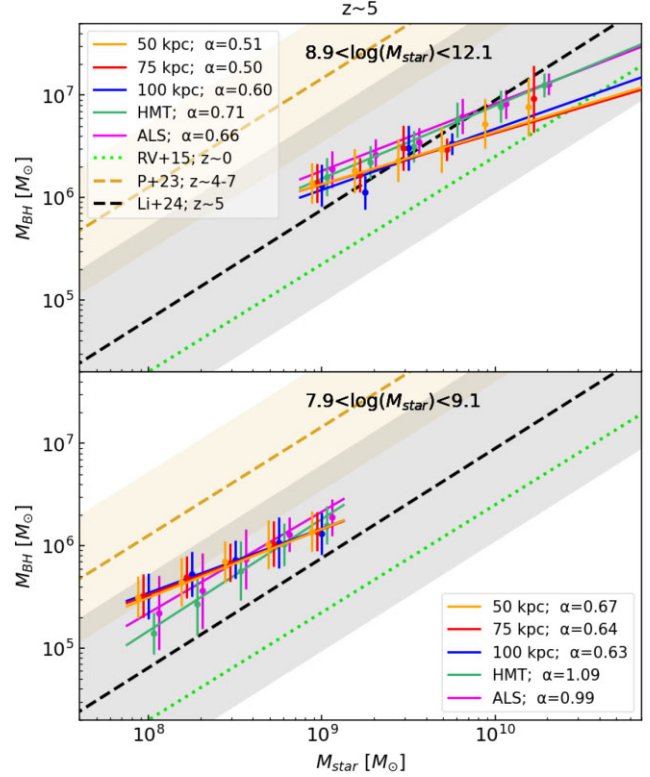
Figure 10. Power-law fits to the $M_{BH} - M_{star}$ relation at $z \sim 5$. Dashed lines depict fits to the JFAINT data with associated dispersion (shaded areas). For reference, we also show the dotted line reporting the RV+15 fit. The indices α are shown in the legend. *(a) Upper panel:* Solid lines indicate the fit results to the median SMBH masses (data points with dispersion) in several stellar mass bins for different seeding models. The stellar mass range covered by the lines corresponds to the fitted interval in the global range. *(b) Lower panel:* As (a), but the fits extend over the low-mass range.

Fig. 7). In terms of scatter, we observe larger values in this stellar mass regime for the Pop III.1 model.

Related to the very-high mass regime of the $M_{BH} - M_{star}$ relation, we see that $\overline{M}_{BH,max10}$ is higher in the Pop III.1 models, i.e. $1 - 2 \times 10^9$ M$_\odot$, than in the HMT or ALS models, where it is $\lesssim 5 \times 10^8$ M$_\odot$. We again attribute this to reduced competition for gas in the Pop III.1 models due to smaller overall numbers of SMBHs. Also, the increased number of BH mergers in HMT and especially in ALS is not significant for the overall growth of the central SMBH, as the majority of mergers can contribute only up to a few percent of the total mass. Recall that the extra seeds in this two schemes are likely to happen in relatively low-mass haloes since the most massive ones are seeded in all the scenarios.

We compare our $z = 0$ results to various observational constraints (see Fig. 9). In particular, we consider the empirical $M_{BH} - M_{star}$ relations obtained from: (1) the $M_{BH} - M_{bulge}$ relation from Kormendy & Ho (2013) (hereafter KH+13), who use dynamical measurements of massive bulge-dominated quiescent galaxies and who find an intrinsic scatter about the relation of about 0.3 dex; (2) the Reines & Volonteri (2015) (hereafter RV+15) relation, which fits the same $M_{BH} - M_{star}$ data set of KH+13, but with an updated mass-to-light ratio, resulting in a lower normalization; (3) the Greene et al. (2020) (hereafter G+20) relation, which considers low-mass ($\sim 10^5$ M$_\odot$) SMBHs and their host galaxies. We note that the inclusion of low-mass objects in the G+20 fit down to stellar masses of $\sim 10^9$M$_\odot$ causes the sample to be sparse and potentially biased for stellar

Table 2. Fitting parameters and derived quantities: the slope α, the intercept $M_{BH,9}$ (at $M_{star} = 10^9 M_\odot$), and dispersion σ are shown at z~5. We also report the average (geometric mean) mass of the 10 most massive BHs.

	z~5				
	50 kpc	**75 kpc**	**100 kpc**	**HMT**	**ALS**
α_{high}	0.75	–	–	0.83	0.78
$\log(M_{BH,9,high}[M_\odot])$	6.08	–	–	6.13	6.19
$\sigma_{high}[dex]$	0.46	–	–	0.39	0.36
α_{low}	0.65	0.60	0.58	0.96	1.04
$\log(M_{BH,9,low}[M_\odot])$	6.07	6.02	6.01	6.13	6.23
$\sigma_{low}[dex]$	0.39	0.38	0.35	0.49	0.58
$\log(\overline{M}_{BH,max10}[M_\odot])$	6.75	6.65	6.56	6.91	6.93

masses below $10^{10} M_\odot$, where the number of objects measured via dynamical methods is small. We note also that low-mass and faint SMBHs are more likely to be missed in observational surveys, potentially biasing the derived relations (e.g. Shankar et al. 2020).

In the range of measured stellar masses from $\sim 10^9 M_\odot$ up to $10^{12} M_\odot$, all theoretical predictions show agreement within the 1-sigma bands of the observational fits provided by RV+15 and by the sample used in G+20. As discussed above, the largest differences between the theoretical models in this regime are in the very high-mass regime, so this may be a promising area for future, more detailed observational tests.

In the low-mass regime, i.e. $\lesssim 10^9 M_\odot$, there are larger differences between the models. As discussed the Pop III.1 models have shallower indices and higher amplitudes than the HMT and ALS models, and these appear to be less in agreement with the RV+15 and G+20 observational results. However, as mentioned the data are relatively sparse in this regime and potentially subject significant systematic uncertainties and observational biases. From the theoretical point of view the precise amplitude and power-law index is also sensitive to choice of a single seed mass of $10^5 M_\odot$. Still, since the models show greatest differences in this regime, we consider than improving the observational constraints at these lower values of M_{star} is a high priority.

3.4.2 High-redshift results

Moving to higher redshifts, in the first five rows of Fig. 8 we show the evolution of the $M_{BH} - M_{star}$ relation of the simulated seeded galaxies from $z \sim 10$ down to $z \sim 2$. To guide the eye, the light green dashed line shows the local relation from RV+15. Table 2 reports power-law fit results for the $z \sim 5$ sample.

As we proceed to higher redshift, the most obvious feature is that there are relatively few massive galaxies and associated highest mass SMBHs. To help quantify this trend, Table 2 reports the results for $\log \overline{M}_{BH,max10}$ for the different seeding schemes at $z \sim 5$. We see that $\log(\overline{M}_{BH,max10} \simeq 7$ for most of the models, dropping to 6.56 for the Pop III.1 model with $d_{iso} = 100$ kpc. This is likely to reflect the fact that this case has the fewest SMBHs and so a reduced sampling of the relatively rare conditions that lead to the strongest growth. In the high-mass regime, the $d_{iso} = 75$ and 100 kpc cases do not form sufficient SMBHs for us to measure the $M_{BH} - M_{star}$ relation. For the other seeding schemes, we see quite similar power-law fits, but with the Pop III.1 $d_{iso} = 50$ kpc case having moderately higher dispersion (see Fig. 10). In the low-mass regime, as at $z = 0$, we see significantly shallower indices in the Pop III.1 models ($\alpha_{low} \simeq 0.6$) compared to the HMT and ALS models ($\alpha_{low} \simeq 1.0$). Furthermore, the Pop III.1 models have smaller dispersions than the HMT and ALS
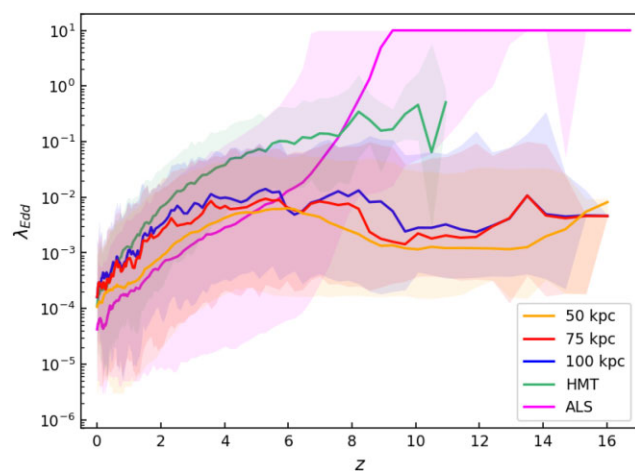

Figure 11. Medians (in log scale, solid lines) of the Eddington ratio λ_{edd} as a function of redshift for the different seeding mechanisms. Shaded areas denote the 1-sigma dispersion of the distributions.

cases. Among the different Pop III.1 models, the effect of varying the isolation distance d_{iso} is relatively hard to distinguish from the $M_{BH} - M_{star}$ relation fits.

Considering the evolution with redshift, among the various seeding schemes, the HMT is the one showing the largest evolution from $z \sim 10$ down to 4 as the process of seeding haloes with SMBHs starts relatively late (i.e. $z \sim 10$, see Paper II). In the ALS seeding model, the BH seeds grow relatively fast and by $z \gtrsim 7$ they have already caught up with the SMBH populations formed from heavy seeds. This is due to the combination of the viscous accretion mode onto the BH and the small seed mass. In fact, seeding with stellar mass BHs allows these objects to accrete several times their own mass as the BH accretion rate goes up to 10 times the Eddington limit and they keep accumulating mass until they become massive enough to self-regulate their own growth primarily via AGN radio-mode feedback (see also Fig. 11).

In Fig. 8 we also compare the theoretical models with recent results obtained from deep *JWST* galaxy surveys where it has been possible to find very faint AGNs otherwise undetected with other facilities (hereafter JFAINT sample). Due to the relatively small volume of our PINOCCHIO box (~ 60 : cMpc per side; see Section 2.1), caution is required when comparing these theoretical results with the full JFAINT sample, which is derived from surveys covering larger volumes. In particular, larger simulation volumes are required to make comparison with the rarest, very luminous quasars.

Focusing on redshifts 4 to 7, we plot data from Maiolino et al. (2024) (twelve low-luminosity AGNs), Harikane et al. (2023) (ten objects), Kocevski et al. (2023) (2 objects), and Übler et al. (2023) (1 object). This JFAINT sample includes sources available from different surveys, specifically from the CEERS (Finkelstein et al. 2023), JADES (Eisenstein et al. 2023) and ERO (Pontoppidan et al. 2022) programmes. In the $z \sim 10$ row we report the single data point (GN-z11) from Maiolino et al. (2024). It is worth noting that the JFAINT sample has been selected by looking for the broad component of the Hα and Hβ lines by means of NIRspec requiring a specific threshold for the full-width half-maximum (FWHM). Additionally, BH masses are measured using a relation connecting the BH mass to the FWHM of the broad line, mainly Hα, calibrated locally using the decomposition of the broad and narrow components of the emission lines (see Harikane et al. 2023; Maiolino et al. 2024). Stellar masses are instead typically estimated
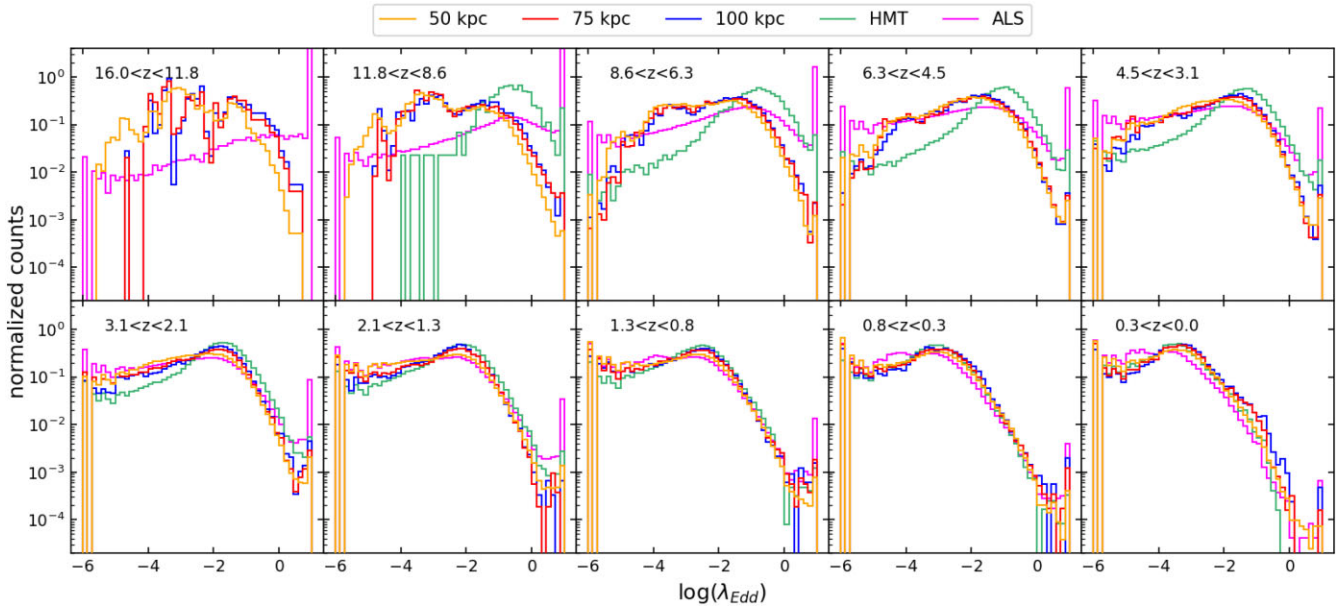
Figure 12. Normalized histograms (in log scale) of the Eddington ratio λ_{edd} for in different redshift bins as a function of the seeding mechanism. The spacing in redshift bins corresponds to a linear spacing in the logarithm of the scale factor a.

via SED fitting, which carries significant uncertainties to corrections related to dust attenuation, assumptions about metallicity, and AGN contribution.

This sample of *JWST*-detected AGNs has been used to estimate the $M_{BH} - M_{star}$ at earlier epochs. Pacucci et al. (2023) (P+23) performed a direct fit of the JFAINT data in order to derive the intrinsic $M_{BH} - M_{star}$ relation at a mean redshift of ~ 5 (golden solid line), concluding that high-z SMBHs tend to be overmassive by a factor of 10–100 with respect to the local relation. This interpretation implies that, even with very massive seeds, super-Eddington accretion episodes are required to frequently occur at high redshift. More recently, Li et al. (2024) (Li+24) have presented a study of the same sample of objects as in P+23 including a detailed analysis of the possible biases. In fact, uncertainties due the measurement of both BH and stellar mass and selection effects caused by flux-limited detection may lead to biased conclusions. According to these authors, the observed data can be explained by assuming that the intrinsic $M_{BH} - M_{star}$ relation is more similar to the local one (e.g. KH+13). Their result, shown by the black line, suggests that local and high-z relations behave in a similar way, where the JFAINT sample is an extremely biased selection towards the most luminous objects.

Our predicted BH masses are, on average, lower by one order of magnitude in BH mass with respect to the most massive BHs in the JFAINT sample (with mean redshift $\simeq 5.2$), while we can reach reasonably high stellar masses by redshift ~ 5. Our $M_{BH} - M_{star}$ relations do not match the P+23 fit, while showing a much better agreement with the estimate of Li+24. If the P+23 results are confirmed as a robust estimate for the true high-$z M_{BH} - M_{star}$ relation, there are two possible arguments that can explain the lack of very massive BHs in our model predictions. On the one hand, the accretion scheme onto the central BH used in this study was calibrated by F20 in the GAEA framework to match AGN bolometric luminosity functions up to redshift ~ 4. The fact that our realizations do not recover such high BH masses may be connected with the physics implemented in the growth model driven by gas momentum loss and viscous accretion, which sets the time-scale of the accretion

rate being inversely proportional to the BH mass as in equation (4). However, at higher redshift cold gas accretion may be expected to be a more continuous process (e.g. Inayoshi et al. 2016) that does not need trigger events such as galaxy mergers and/or disc instabilities to happen. If true, this could lead SMBHs to grow on shorter time-scales and/or at higher efficiencies than we have so far implemented (see the discussion in Section 2.2.1).

Additionally, the limited size of our PINOCCHIO box also limits our ability to sample extreme, rare objects that undergo the fastest, most efficient accretion. This volume effect is particularly evident by looking at the top row at $z \sim 10$, where only single objects can occasionally match the GN-z11 data point within its error bars. We note that our simulated volume is at least a factor of 10 smaller than those probed by the JADES and CEERS programs.

Furthermore, the measurements of BH masses using local calibrations may be significantly biased upward (by up to one order of magnitude), as suggested recently by Abuter et al. (2024). Other considerations are that for the Pop III.1 and HMT models we seed galaxies with a delta function distribution of BH mass at $10^5 M_\odot$. More realistically, we would include a range of masses with dispersion, and this would enhance the chance to obtain a few, larger SMBH masses.

3.5 Eddington ratios

Here we examine the distribution of Eddington ratios, λ_{edd}, that are present in our modelled SMBH populations. Figs 11 and 12 show in different formats the distribution of λ_{edd} across different seeding models as a function of redshift. The solid lines in Fig. 11 show the median λ_{edd} of the different models, with shaded areas being the 1σ dispersion as a function of redshift. Fig. 12 shows the normalized histograms of λ_{edd} in ten redshift bins. For Pop III.1 models, the distributions, including median values, of λ_{edd} are relatively similar. We do notice that, especially at higher redshifts, the cases with larger d_{iso} have a higher proportion of higher accretion rate SMBHs. Comparing high and low redshifts, at higher redshifts the SMBHs tend to have higher accretion rates, with a median λ_{edd} of $\sim 10^{-3}$ to

10^{-2} down to $z \sim 1$ for $d_{iso} = 75$ and $100\,\text{kpc}$ cases and $z \sim 2$ for $d_{iso} = 50\,\text{kpc}$. After this, SMBHs start to self-regulate their growth via AGN feedback. This decreases the available gas which in turn lowers the average accretion to $\lambda_{edd} \sim 10^{-4}$ by $z \sim 0$. However, the histograms in Fig. 12 show that the SMBHs have a tail towards accretions close to the Eddington limit (or even super-Eddington), which would manifest as luminous AGN, including quasars.

On the other hand, the HMT and ALS models exhibit different distributions of λ_{edd}. In the case of HMT, the BH seeds appear at lower redshift ($z \sim 10$) in already massive haloes where a substantial amount of gas available for accretion has gathered during its previous history. At this point, the central BHs are able to accrete efficiently resulting in λ_{edd} of about an order of magnitude larger than in the Pop III.1 models. However, below $z \sim 3$ the HMT BHs tend to align with the behaviour of the Pop III.1 populations.

For the ALS model, the BH seeds are significantly lower in mass than the other seeding models considered in this study. This explains the fact that down to $z \sim 8$ the large majority of BHs are accreting at super-Eddington rates (limited at 10 times as a basic model assumption). In fact, in the viscous accretion prescription the accretion rate is proportional to the ratio between the BH gas reservoir and the BH mass. Until the ALS BHs reach the supermassive regime, this ratio takes values much larger with respect to the other models, explaining the trends observed in Figs 12 and 11. At lower redshifts, these systems tend to run out of gas available for BH accretion, as all haloes are seeded (e.g. see the BHMF in Fig. 7). We note that by $z \sim 2$ and down to the local Universe, all the models have generally similar distributions, although the ALS model retains an excess of very high, super-Eddington accretors, mostly being low- and intermediate-mass BHs.

4 SUMMARY AND CONCLUSIONS

In this work, we have introduced a novel semi-analytic approach that accounts for different SMBH seeding scenarios within theoretical models of galaxy formation and evolution. It utilizes merger trees generated by the PINOCCHIO code for dark matter haloes, extends them by incorporating subhaloes, and then applies the GAEA semi-analytic model to populate these haloes with observable galaxies. This approach allows us to investigate a wide range of galaxy properties by adjusting various parameters governing galaxy formation without expensive N-body and/or hydrodynamical simulations. The evolution of subhaloes and their merging with the main haloes is implemented via physically motivated models that have been calibrated on simulations.

We first adapted the structure of PINOCCHIO merger trees to the Millennium simulation format by adding information about the subhaloes. We assume a spatial distribution for subhaloes following a NFW density profile (Navarro et al. 1997), statistical prescriptions for the angular momentum (Zentner et al. 2005; Birrer et al. 2014), and a subhalo survival time since accretion (Boylan-Kolchin et al. 2008; Berner et al. 2022). This ensures that the GAEA model will be able to run on PINOCCHIO-generated halo merger trees. We calibrated this method on a Millennium-like PINOCCHIO box making sure that we fed the semi-analytic model with a consistent halo mass function. By anchoring the calibration to the local observed GSMF, we estimated a total survival time for satellite galaxies, which is tuned to reproduce the exponential cut-off of the high-mass end of the predicted GSMF at $z \sim 0$. This approach makes it possible to apply our fully semi-analytic pipeline to a variety of scientific cases beyond the scope of this paper.

We have primarily focused on the impact of implementing different mechanisms for seeding SMBHs, especially focusing on the Pop III.1 model, which postulates a new mechanism for the formation of all SMBHs. We have investigated three values of the isolation distance that is needed for a given minihalo to be a Pop III.1 source. For comparison, we have examined the HMT used by the Illustris-TNG simulations in which every halo exceeding a mass of $7.1 \times 10^{10}\,\text{M}_\odot$ is seeded with a BH of mass $1.4 \times 10^5\,\text{M}_\odot$. As another example case, we also considered predictions for the standard seeding scheme implemented in GAEA based on ALS. Here, the initial mass of the BH seed scales with the initial halo mass, resulting in light seeds of the order of stellar mass BHs.

Within our framework, we have explored the implications of this set of seeding models when applied to cosmological volumes in a galaxy formation and evolution framework down to low redshifts. Unlike other astrophysical models, the Pop III.1 scenario presents the earliest and least clustered distribution of seeds, affording relatively longer periods of time for black hole growth via accretion, reducing the need for sustained modes of super-Eddington accretion.

Our main findings are the following:

(i) For the Pop III.1 models, SMBH seeds are predominantly abundant in massive galaxies, with the occupation fraction increasing as d_{iso} decreases. By $z \sim 0$, the occupation fraction reaches unity for halo masses above $10^{13}\,\text{M}_\odot$ across all models. AGN feedback significantly influences the thermal state of the gas and the SFR, quenching seeded galaxies by $z \sim 0$. The observational measurements of the occupation fraction in the local Universe as a function of stellar mass suggest that $d_{iso} < 75$ kpc. In contrast, the HMT and ALS scheme produce too many BHs in systems with $M_{star} \sim 10^{9-10}\,\text{M}_\odot$.

(ii) The AGN radiomode feedback affects the shape of the GSMF by decreasing the SFR in massive galaxies, if hosting a SMBH, and causing the exponential cut-off at the high-mass end. At $z \sim 0$, the low-mass end of the GSMFs obtained from Pop III.1 models is generally similar to the predictions of the HMT and ALS models and with the observations, as in this regime the number densities are regulated by SN feedback. Above few $\times 10^{13}\,\text{M}_\odot$, smaller isolation distances are favoured to reproduce the quenching of the majority of massive galaxies, consistent with $d_{iso} \lesssim 75$ kpc scenarios.

(iii) The slope of the BHMF at low SMBH masses is found to be a crucial way to distinguish different seeding models. Our favoured cases with $d_{iso} < 75$ kpc match the high-mass end of the BHMF and is in reasonable agreement with estimates at the low-mass end. However, it should be noted that the observational constraints are relatively uncertain in this regime and many lower mass SMBHs may be missed in current surveys.

(iv) The predicted $M_{BH} - M_{star}$ relations at redshift zero show some differences between the models. The main differences are a trend for the Pop III.1 models to have modestly steeper indices in the very high-mass regime, i.e. with $M_{star} > 10^{11}\,\text{M}_\odot$. Larger differences are present in the low-mass regime, i.e. with $M_{star} < 10^9\,\text{M}_\odot$, which reflects the imprint of the assumed mass scale of the seeds, i.e. $M_{BH} = 10^5\,\text{M}_\odot$. We note that so far we have made very simple assumptions for this seed mass. We also note that the observational data in the regime are subject to significant uncertainties due to the difficulty of obtaining a complete census of SMBHs in this regime.

(v) At high redshifts, comparison of the model $M_{BH} - M_{star}$ relations with observational constraints derived from *JWST*-detected AGN candidates remains open to debate as the probed ranges of BH and stellar masses are likely biased upwards by the most luminous objects and not well sampled by the limited volume of the simulation considered in this study.

(vi) The distribution of λ_{edd} suggests that, within the viscous accretion model for the BHs adopted in GAEA, massive seeds do not grow very efficiently in their early phases, while light seeds tend to accrete at the maximum rate allowed (i.e. 10 times Eddington).

(vii) All three local, $z \sim 0$ metrics of occupation fraction as a function of the galaxy stellar mass, GSMF, and BHMF suggest a constraint of $d_{iso} < 75$ kpc. Such a value places a constraint on physical models for the isolation distance, e.g. due to photoionization from the Pop III.1 source.

Expanding on this final point, a reference scale for radiative feedback from the Pop III.1 sources themselves is the radius of the Strömgren sphere of a supermassive, $\sim 10^5\,M_\odot$ protostar, which may have a final phase of evolution that involves being on or close to the ZAMS for several Myr. Such a star is expected to have a H-ionizing photon luminosity of $S \sim 10^{53}$ H-ionizing photons per second and to heat its H II region to temperatures of $T \sim 30\,000$ K. Then, the radius of the H II region adopting a mean intergalactic medium density is

$$r_{\rm HII} = 61.3\, S_{53}^{1/3}\, T_{3e4}^{0.27} \left(\frac{n_{\rm H}}{n_{\rm H, z=30}} \right)^{-2/3} \text{ kpc}, \tag{15}$$

where $S_{53} \equiv S/(10^{53}\,{\rm s}^{-1})$, $T_{3e4} \equiv T/(3 \times 10^4\,{\rm K})$, and $n_{\rm H, z=30}$ is the mean number density of H nuclei in the IGM at $z = 30$. We note that this mean density scales as $(1 + z)^3$, so by $z = 20$, the mean density drops by a factor of 0.310, which would increase $r_{\rm HII}$ by a factor of 2.18. We also note that the actual size of the H II region may be limited by R-type expansion, with the time-scale to establish ionization equilibrium being longer than 10 Myr. This would tend to make the size of the H II region somewhat smaller than the estimate given in equation (15). In spite of these uncertainties, we consider the close correspondence of this ionization feedback scale with the constraint on $d_{iso} < 75$ kpc derived from our semi-analytic modelling of galaxy evolution and SMBH growth to indicate that this feedback process may well play an important role in setting the conditions for Pop III.1 supermassive star and SMBH formation, with the regions affected by the H II regions forming lower mass Pop III.2 stars (Greif & Bromm 2006; Johnson & Bromm 2006) (see Section 1).

The next major step that is needed to enable further comparison of model results with observational data is to make predictions for the luminosities of the galaxies and AGN in these simulations. This is the focus of a follow-up paper to this work (Cammelli et al., in prepaparation). Another promising avenue is to utilize the developed SMBH growth models to make predictions for the gravitational wave emission from these different seeding scenarios (Singh et al., in preparation).

ACKNOWLEDGEMENTS

DATA AVAILABILITY

The data underlying this article will be shared on reasonable request to the corresponding author.

REFERENCES

Abuter R. et al., 2024, Nature, 627, 281
Banik N., Tan J. C., Monaco P., 2019, MNRAS, 483, 3592
Barber C., Schaye J., Bower R. G., Crain R. A., Schaller M., Theuns T., 2016, MNRAS, 460, 1147
Begelman M. C., Volonteri M., Rees M. J., 2006, MNRAS, 370, 289
Bell E. F., McIntosh D. H., Katz N., Weinberg M. D., 2003, ApJ, 149, 289
Berner P., Refregier A., Sgier R., Kacprzak T., Tortorelli L., Monaco P., 2022, J. Cosmol. Astropart. Phys., 2022, 002
Bertocco S. et al., 2020, in Pizzo R., Deul E. R., Mol J. D., de Plaa J., Verkouter H., eds, Astronomical Society of the Pacific Conference Series. Vol. 527, p. 303
Bhowmick A. K. et al., 2022, MNRAS, 516, 138
Bhowmick A. K. et al., 2024a, MNRAS, 533, 1907
Bhowmick A. K., Blecha L., Torrey P., Weinberger R., Kelley L. Z., Vogelsberger M., Hernquist L., Somerville R. S., 2024b, MNRAS, 529, 3768
Bhowmick A. K. et al., 2024c, MNRAS, 531, 4311
Binney J., Tremaine S., 1987, Galactic Dynamics. Princeton Univ. Press, Princeton, NJ, p. 747
Birrer S., Lilly S., Amara A., Paranjape A., Refregier A., 2014, ApJ, 793, 12
Boylan-Kolchin M., Ma C.-P., Quataert E., 2008, MNRAS, 383, 93
Brennan R., Choi E., Somerville R. S., Hirschmann M., Naab T., Ostriker J. P., 2018, ApJ, 860, 14
Bromm V., Loeb A., 2003, ApJ, 596, 34
Bundy K., Ellis R. S., Conselice C. J., 2005, ApJ, 625, 621
Chandrasekhar S., 1943, ApJ, 97, 255
Chon S., Hirano S., Hosokawa T., Yoshida N., 2016, Apj, 832, 134
Cole S. et al., 2001, MNRAS, 326, 255
Croton D. J. et al., 2006, MNRAS, 365, 11
Dayal P., Rossi E. M., Shiralilou B., Piana O., Choudhury T. R., Volonteri M., 2019, MNRAS, 486, 2336
De Lucia G., 2019, Galaxies, 7, 56
De Lucia G., Blaizot J., 2007, MNRAS, 375, 2
De Lucia G., Boylan-Kolchin M., Benson A. J., Fontanot F., Monaco P., 2010, MNRAS, 406, 1533
De Lucia G., Fontanot F., Wilman D., Monaco P., 2011, MNRAS, 414, 1439
De Lucia G., Tornatore L., Frenk C. S., Helmi A., Navarro J. F., White S. D. M., 2014, MNRAS, 445, 970
De Lucia G., Hirschmann M., Fontanot F., 2019, MNRAS, 482, 5041
De Lucia G., Fontanot F., Xie L., Hirschmann M., 2024, A&A, 687, A68
Delvecchio I. et al., 2020, ApJ, 892, 17
Devecchi B., Volonteri M., 2009, ApJ, 694, 302
Di Matteo T., Angles-Alcazar D., Shankar F., 2023, preprint (arXiv:2304.11541)
Drory N., Bender R., Feulner G., Hopp U., Maraston C., Snigula J., Hill G. J., 2004, ApJ, 608, 742
Eisenstein D. J. et al., 2023, preprint (arXiv:2306.02465)
Ferrarese L., 2002, ApJ, 578, 90
Finkelstein S. L. et al., 2023, ApJ, 946, L13
Fiore F. et al., 2017, A&A, 601, A143
Fontana A. et al., 2006, A&A, 459, 745
Fontanot F., Monaco P., Cristiani S., Tozzi P., 2006, MNRAS, 373, 1173
Fontanot F., De Lucia G., Hirschmann M., Bruzual G., Charlot S., Zibetti S., 2017a, MNRAS, 464, 3812
Fontanot F., Hirschmann M., Lucia G. D., 2017b, ApJ, 842, L14
Fontanot F., De Lucia G., Xie L., Hirschmann M., Bruzual G., Charlot S., 2018, MNRAS, 475, 2467
Fontanot F. et al., 2020, MNRAS, 496, 3943
Fontanot F. et al., 2024, A&A, 686, A302
Freese K., Ilie C., Spolyar D., Valluri M., Bodenheimer P., 2010, ApJ, 716, 1397
Gao L., De Lucia G., White S. D. M., Jenkins A., 2004, MNRAS, 352, L1
Granato G. L., Zotti G. D., Silva L., Bressan A., Danese L., 2004, ApJ, 600, 580
Greene J. E., Strader J., Ho L. C., 2020, ARA&A, 58, 257
Greif T. H., Bromm V., 2006, MNRAS, 373, 128

Habouzit M., Volonteri M., Latif M., Dubois Y., Peirani S., 2016, MNRAS, 463, 529

Harikane Y. et al., 2023, ApJ, 959, 39

Henriques B. M. B., White S. D. M., Thomas P. A., Angulo R., Guo Q., Lemson G., Springel V., Overzier R., 2015, MNRAS, 451, 2663

Hirschmann M., De Lucia G., Fontanot F., 2016, MNRAS, 461, 1760

Inayoshi K., Haiman Z., Ostriker J. P., 2016, MNRAS, 459, 3738

Inayoshi K., Visbal E., Haiman Z., 2020, ARA&A, 58, 27

Jiang Y.-F., Stone J. M., Davis S. W., 2019, ApJ, 880, 67

Johnson J. L., Bromm V., 2006, MNRAS, 366, 247

Kocevski D. D. et al., 2023, ApJ, 954, L4

Kormendy J., Ho L. C., 2013, ARA&A, 51, 511

Lacey C., Cole S., 1993, MNRAS, 262, 627

Li J. et al., 2024, preprint (arXiv:2403.00074)

Madau P., Rees M. J., 2001, ApJ, 551, L27

Maiolino R. et al., 2024, A&A, 691, A145

Maiolino R. et al., 2024, Nature, 627, 59

Matteo T. D., Colberg J., Springel V., Hernquist L., Sijacki D., 2008, ApJ, 676, 33

McKee C. F., Tan J. C., 2008, ApJ, 681, 771

Miller B. P., Gallo E., Greene J. E., Kelly B. C., Treu T., Woo J.-H., Baldassare V., 2015, ApJ, 799, 98

Monaco P., Fontanot F., 2005, MNRAS, 359, 283

Monaco P., Theuns T., Taffoni G., 2002, MNRAS, 331, 587

Montero P. J., Janka H.-T., Müller E., 2012, ApJ, 749, 37

Munari E., Monaco P., Sefusatti E., Castorina E., Mohammad F. G., Anselmi S., Borgani S., 2017, MNRAS, 465, 4658

Mutlu-Pakdil B., Seigar M. S., Davis B. L., 2016, ApJ, 830, 117

Natarajan A., Tan J. C., O'Shea B. W., 2009, ApJ, 692, 574

Navarro J. F., Frenk C. S., White S. D. M., 1997, ApJ, 490, 493

Nguyen D. D. et al., 2019, ApJ, 872, 104

Pacucci F., Nguyen B., Carniani S., Maiolino R., Fan X., 2023, ApJ, 957, L3

Panter B., Jimenez R., Heavens A. F., Charlot S., 2007, MNRAS, 378, 1550

Pérez-González P. G. et al., 2008, ApJ, 675, 234

Planck Collaboration VI 2020, A&A, 641, A6

Pontoppidan K. M. et al., 2022, ApJ, 936, L14

Portegies Zwart S. F., Baumgardt H., Hut P., Makino J., McMillan S. L. W., 2004, Nature, 428, 724

Press W. H., Schechter P., 1974, ApJ, 187, 425

Rees M. J., 1978, The Observatory, 98, 210

Reines A. E., Volonteri M., 2015, ApJ, 813, 82

Ricarte A., Natarajan P., 2018, MNRAS, 474, 1995

Rindler-Daller T., Montgomery M. H., Freese K., Winget D. E., Paxton B., 2015, ApJ, 799, 210

Sassano F., Schneider R., Valiante R., Inayoshi K., Chon S., Omukai K., Mayer L., Capelo P. R., 2021, MNRAS, 506, 613

Shankar F. et al., 2020, Nat. Astron., 4, 282

Sijacki D., Springel V., Di Matteo T., Hernquist L., 2007, MNRAS, 380, 877

Singh J., Monaco P., Tan J. C., 2023, MNRAS, 525, 969

Somerville R. S., Davé R., 2015, ARA&A, 53, 51

Somerville R. S., Primack J. R., Faber S. M., 2001, MNRAS, 320, 504

Spinoso D., Bonoli S., Valiante R., Schneider R., Izquierdo-Villalba D., 2023, MNRAS, 518, 4672

Spolyar D., Freese K., Gondolo P., 2008, Phys. Rev. Lett., 100, 051101

Springel V. et al., 2005, Nature, 435, 629

Taffoni G., Becciani U., Garilli B., Maggio G., Pasian F., Umana G., Smareglia R., Vitello F., 2020, in Pizzo R., Deul E. R., Mol J. D., de Plaa J., Verkouter H., eds, Astronomical Society of the Pacific Conference Series. Vol. 527, p. 307

Takeo E., Inayoshi K., Ohsuga K., Takahashi H. R., Mineshige S., 2019, MNRAS, 488, 2689

Tan J. C., McKee C. F., 2004, ApJ, 603, 383

Trebitsch M. et al., 2021, A&A, 653, A154

Tremmel M., Karcher M., Governato F., Volonteri M., Quinn T. R., Pontzen A., Anderson L., Bellovary J., 2017, MNRAS, 470, 1121

Trinca A., Schneider R., Valiante R., Graziani L., Zappacosta L., Shankar F., 2022, MNRAS, 511, 616

Übler H. et al., 2023, A&A, 677, A145

Van Den Bosch F. C., Aquino D., Yang X., Mo H. J., Pasquali A., McIntosh D. H., Weinmann S. M., Kang X., 2008, MNRAS, 387, 79

Vogelsberger M. et al., 2014, MNRAS, 444, 1518

Volonteri M., 2010, A&AR, 18, 279

Volonteri M., Natarajan P., Gültekin K., 2011, ApJ, 737, 50

Volonteri M., Dubois Y., Pichon C., Devriendt J., 2016, MNRAS, 460, 2979

Volonteri M., Habouzit M., Colpi M., 2021, Nat. Rev. Phys., 3, 732

Wang F. et al., 2021, ApJ, 907, L1

White S. D. M., Frenk C. S., 1991, ApJ, 379, 52

Wise J. H., Regan J. A., O'Shea B. W., Norman M. L., Downes T. P., Xu H., 2019, Nature, 566, 85

Xie L., De Lucia G., Hirschmann M., Fontanot F., Zoldan A., 2017, MNRAS, 469, 968

Xie L., De Lucia G., Hirschmann M., Fontanot F., 2020, MNRAS, 498, 4327

Zentner A. R., Berlind A. A., Bullock J. S., Kravtsov A. V., Wechsler R. H., 2005, ApJ, 624, 505

Zoldan A., De Lucia G., Xie L., Fontanot F., Hirschmann M., 2019, MMRAS, 487, 5649

APPENDIX A: GALAXY SURVIVAL TIME

As discussed in Section 2.4, we adopt the sum of two different time scales when dealing with galaxy mergers. First, we estimate the time the subhalo will survive within the main halo group, which has been evaluated via comparison against N-body simulations Berner et al. (2022). Secondly we keep track of the orphan galaxies by adding a second time which mimics the phase during which a galaxy would orbit around the central one and eventually merge with it. In Fig. A1 we present the estimated total survival time of satellite galaxies as a function of the halo mass ratio calculated at the halo merging time taken from PINOCCHIO using the values reported in equation (12). In particular, we report data from the seeded halos for the $d_{iso} = 50$ kpc case. This distribution of points has been calibrated to reproduce the Millennium one as obtained from the standard implementation of GAEA. The impact of the total survival time proposed in equation (10)) and (11) introduces a dual dependence. Mergers with comparable halo masses tend to last on average few Gyr and typically this happens when the two merging halos belong to the low mass end of the halo mass function. As one increases the mass of the primary halo, it will eventually merge with even smaller halos. For these cases the total survival time will overshoot the age of the Universe and the two structures will never merge. This is in agreement with findings in simulations (Somerville & Davé 2015). The more comparable are the encounters, the more efficient we expect the interaction to be
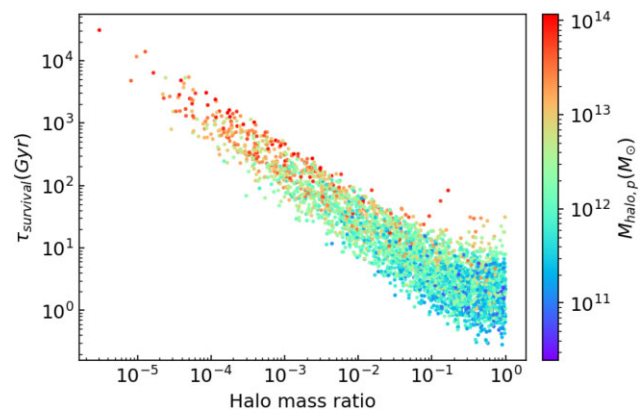

Figure A1. Estimated total survival time in Gyr for seeded haloes for the $d_{iso} = 50$ kpc case as a function of the halo mass ratio and colour coded with the mass of the most massive (primary) halo.

(i.e. via dynamical friction, ram pressure stripping, tidal disruption forces, etc.), resulting in a shorter time scale. Conversely, on average small galaxies joining a massive central galaxy group are thought to undergo very minor physical effects, ending up orbiting around the central galaxy undisturbed for tens or thousands of Hubble times.

APPENDIX B: CALIBRATED GALAXY STELLAR MASS FUNCTION

The galaxy survival time introduced in Section 2.3 and showed in Appendix A as a function of the halo mass ratio plays a crucial role in shaping the GSMF. Once again we note that our calibration process has been performed aiming at reproducing the Millennium-based result at redshift 0, and not against observational data. In this appendix we show the results from the calibrated GSMFs at redshifts $z \sim 1$ to 3. In particular we emphasize that our PINOCCHIO-based GSMF well reproduces the Millennium-based predictions up to $z \sim 3$ and above. The agreement between the two different trends is depicted in Fig. B1, where we indicate Millennium- and PINOCCHIO-based GSMFs in blue and red, respectively. This supports the goodness of our calibration of the galaxy survival time in order to obtain reliable model galaxy catalogues.
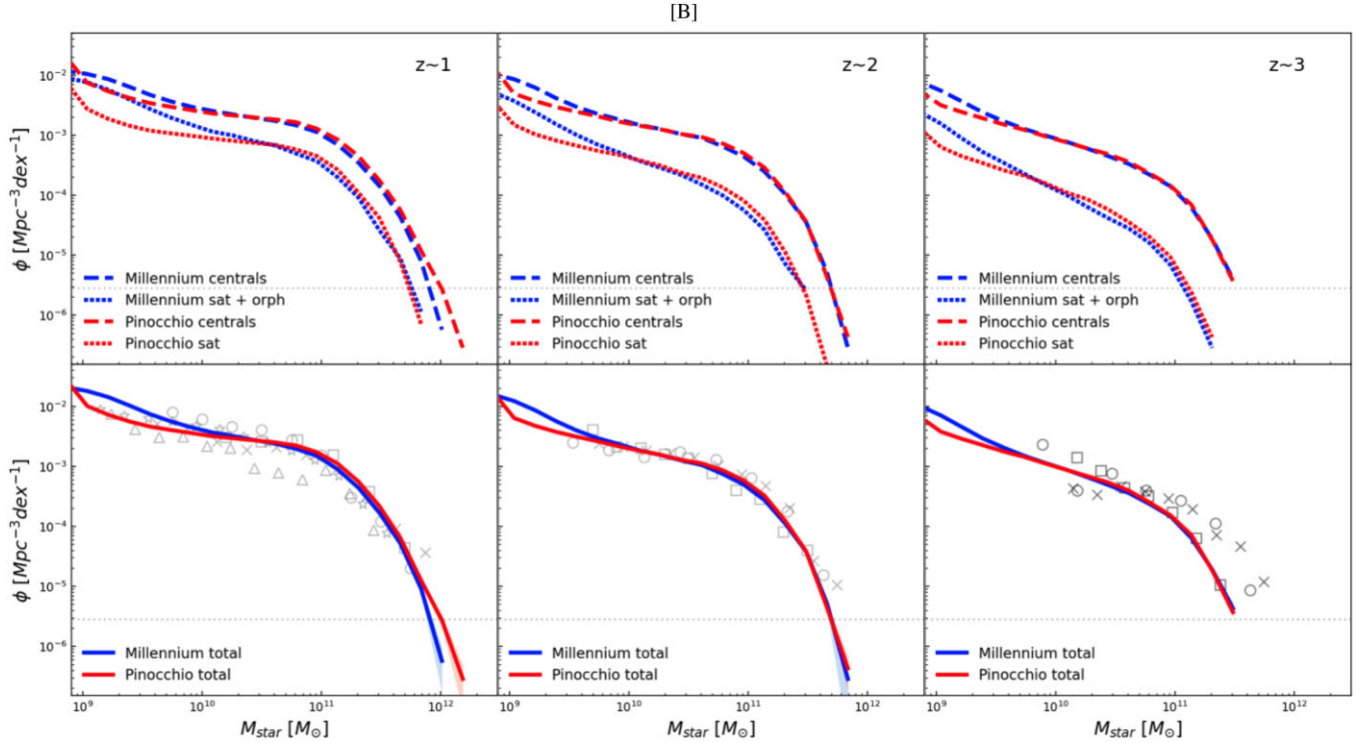

Figure B1. GSMF predictions based on the Millennium simulation box compared to the GSMF extracted from our Millennium-like PINOCCHIO box run used for the calibration of the merging times (see Section 2.4). *Upper panels*: satellite and central galaxies contributions to the GSMF are reported separately in dotted and dashed lines, respectively. *Lower panels*: total GSMFs. Various symbols show observational estimates as reported in Fig. 2.

This paper has been typeset from a TEX/LATEX file prepared by the author.